

Copyright

By

Kelvin Le

2014

The Thesis Committee for Kelvin Le

Certifies that this is the approved version of the following thesis:

**High Performance Wireless Bio-impedance Measurement System**

**APPROVED BY**

**SUPERVISING COMMITTEE**

**Supervisor:** \_\_\_\_\_

Jonathan W. Valvano

\_\_\_\_\_

John Pearce

**High Performance Wireless Bio-impedance Measurement System**

**by**

**Kelvin Le, B.S**

**Thesis**

Presented to the Faculty of the Graduate School of

The University of Texas at Austin

in Partial Fulfillment

of the Requirements

for the Degree of

**Master of Science in Engineering**

**The University of Texas at Austin**

**December 2014**

## **Acknowledgements**

I remember Professor Eric Swanson once said that “there is no way for you to predict where you will be in five or ten years”, and I think there is some truth in that. If someone was to tell me ten years ago that I was going to graduate with a degree in electrical engineering, never alone receiving a fellowship along the way, I would tell them they were out of their minds. I was just an above average student in high school. Luckily, I met the right people along the way who believed in me and encouraged me to aim high. Go for the moon sort of things. The further along I got the more confident I became and ultimately I became my own advocate. I have always thought of myself as the champion for the average folks. I knew that I was not the smartest kid in school but I believed that if I just work a bit harder and study just a bit smarter then maybe I might have a chance at greatness. I want to be a role model to other people and show them that they do not have to be an Einstein to achieve great things in their lives. Sometimes, all people need is just a mentor—someone that gives them that extra kick to get going when they needed the most. That is partly why I enjoy making YouTube video tutorials helping people learn on my free time.

I considered myself very fortunately to have met Dr. Wei R. Chen when I came to college. The University of Central Oklahoma engineering department is not a very big one but boy did I pick the right professor. I have owed a great debt to this man who has taught me almost everything I needed to succeed in school and in life. I still remember him telling me “Kelvin, you’ll need to learn how to write, and you’ll need to do it well. I know you don’t like to write, but it is really important that you do.” I believe that my

greatest strength, if any, is that I'm a good listener. Under his supervision, I have conducted independent research and published a number of papers; two of which I was the first author and one was a peer-reviewed journal. Something I could not have imagined doing just a few years back. Dr. Chen is one of those few people that has the natural ability to change lives. A humble and charismatic teacher, he constantly elevates his students to new heights they themselves thought unattainable. I still have fond memories of the days when we would have these so called "writing sweatshops" just before the Thanksgiving weekend. Imagine a room crowded with ten or fifteen students just typing away on their computers. I compared these experiences to getting a flu shot: it is slightly unpleasant but I knew it was for my own good. Like a prophet, he was never wrong.

Going to graduate school far away from home is not an easy thing to do to say the least. Luckily, I have kind and loving parents who have always been there for me. They are my lifelines, and I don't know if I could have achieved what I achieved without their unconditional support. I don't think words can do justice to describe how fortunate I am to have such caring and loving parents. I confess, living far away from home has made me realize how important my family is to me and how much I love them. Whenever I feel down, I would just call my mom and she would know just what to say to make it all better. She is the star that lights up my sky. Rain or snow, she has always been there for me. I still remember the days back in Vietnam when she would take me to school on the back of her bicycle. She would look after me and made sure I did not go to school on an empty stomach. I was clueless at the time and didn't realize how lucky I was. There

were mornings when I would fuss about going to school but she had always managed to convince me otherwise. If there is one thing that is sacred in our family, it is a good education, and you just don't fool around with that. Back then, my dad had a job far from home, so it was my mom who had to practically raise three children on her own. She did what she could to put clothes on our backs and food on our tables. Now that I'm older, I realized that back then we were, in many ways, protected and sheltered from the harsh living conditions of Vietnam. We were considered the fortunate ones. When I was little, I did not get to spend a lot of time with my dad because of his long-distance job. However, I still remember and treasure the many good times we shared together. Back then, when we came to visit him on the weekends, I still vividly remember, he would prepare his one and only famous dish: baby back ribs with marinara-like sauce. I asked my mom if she could top that. In all seriousness, my dad is a very hard working man who does what he can to provide for his family and you can't really ask for more than that.

My uncle Khanh and his family have always been very supportive in various aspects of my life. When our family first moved to the U.S. in 1999, they welcomed us to their home with open arms and hearts. My uncle is one of those selfless folks who put others first before himself. He is very protective. He made sure that my brother and I did not get picked on in school and have everything we needed to succeed. When I left Oklahoma City for school in Austin he made sure that I have enough money for the long drive. I will always be grateful for the things he and family have done for us. This thesis is my way of showing my gratitude.

Throughout graduate school, I was fortunate enough to have taken three of Dr. Pearce's courses: biomedical instrumentation, analog electronics, and therapeutic heating. Dr. Pearce has taught me how to design analog circuits with common sense, and he makes it look easy too. "You can't use a 1- $\mu$ F capacitor for your filter it is just not realistic", he once said. We used to joke around (and still do) about one of his famous quotes "I can't do circuits in the air!" Well, I guess that is the only thing that he can't do because Dr. Pearce is one of those people who knows a whole lot and with great depth too. If you have a circuit problem he will just prescribe you a new circuit to try out. It's the doctor's orders. In addition, if there is one secret weapon that Dr. Pearce has it is his course notes. I truly enjoy reading his course notes in 374k and 338k where he has these so called "Designer's Trick" sections that make you think about real-life design issues. Since it is a "trick" I have always felt like I'm one of the few fortunate students who found awesome design secrets. In addition, he has taught me how to debug analog circuits, "unlike the justice system, everything is guilty until proven innocent," and how to model systems, "garbage in garbage out." Above all, Dr. Pearce has taught me how to be a practical designer and that is something that I will never forget.

It took me awhile to get a feel for Dr. Valvano teaching style partly because I never got a chance to take one of his famous embedded classes—now available worldwide. After getting to know him better over the years, I have found that Dr. Valvano is a very kind and nurturing teacher. Even though sometimes he likes to put me on the spot and make me draw things (just because it is a Friday), I would still describe him as an organic teacher. He enjoys developing his students in an organic manner—

never too pushy. He has always encouraged me to try new things. In addition, he has taught me how to “always have a backup plan for your backup plan” and “expect your first design not to work.” And with quotes like “it’s always the connector” that makes me think twice before trying out new designs. You can see the impact he has had by just looking at the achievements of his former students.

Dr. Marc Feldman is one of the hardest working people I know and with a great deal of energy to match. He is constantly organizing and challenging his team to push just a little harder and just a little faster. Dr. Feldman is the clock that synchronizes the research effort that keeps our research group on task. I believe he truly has the students’ interest at heart.

I would like to also thank the following people for their relentless support and words of encouragement through the years:

*Lucas Holt* for being such an expert on just about anything. Lucas is my go-to-guy for help—especially with programming and DSP. He is what I call a force multiplier. A hard worker/machine, he constantly pushes himself and other people around him to succeed and with pace. With his help, I was able to expedite my research project in ways that I couldn’t possibly done alone. Lastly, for showing me good times at “The Local.”

*Andrew Wang* for being such a good friend, letting me hangout with him and his other friends downtown, and teaching me how to swim (he is really fast). Andrew is one of those people that you can talk to on just about anything. Like a teddy bear, he is

always there to listen and help. Lastly, we share a similar taste in music, which is nice since we are usually together in lab.

*Dr. Anil Kottam* for keeping good company for some of the trips to San Antonio and helping me getting started with the surface probe calibration process. Lastly, he dresses really nice.

*Dr. John Porterfield* for his many words of advice and encouragement early on regarding graduate school and research.

*Dr. Erik Larson* for his support with building the surface probe and navigating through the design documentation.

*Danny Escobedo* is one of the animal surgeons in San Antonio that helped me conduct animal experiments early on in my graduate studies.

*Bryan Brumm* for showing me “Taco Joint”, which has become my favorite place to eat tacos.

*Kaarthik Rajendran* for being a good friend and lab partner. Kaarthik is one of the few people that just love to learn and be in school.

*Sam Oyetungi* for being an awesome friend and study buddy. I never had a study buddy before until Sam came along. We took both analog IC and mixed signals together back in the spring of 2014. He’s really good at keeping things light and I especially enjoy his company. I miss having him around the lab since we moved out of ENS. I remember he used to call me the “cookie monster” that I was.

*Dr. Deji Akinwande* for being an awesome analog IC professor that taught me “there is no free lunch” and good design practices.

*Dr. Nan Sun* for his words of encouragement and valuable feedbacks.

## Abstract

# High Performance Wireless Bio-impedance Measurement System

Kelvin Le, M.S.E.

The University of Texas at Austin, 2014

Supervisor: Jonathan W. Valvano

A high performance, wireless bio-impedance measurement system has been designed for the purpose of monitoring essential electrical properties of the heart during cardiac ablation. The system is broken into three parts: a spring-loaded device to house a tetrapolar surface probe and sensors, a wireless bio-impedance measurement system, and a desktop base station for graphical data display and acquisition. The system is specifically designed for a tetrapolar-electrode configuration where the two outer electrodes served as a current source operating at 20 kHz with an amplitude of 100  $\mu$ Arms and the two inner electrodes served as voltage sensing electrodes. In addition, the system also has a dedicated channel for current sense. The system is designed to be modular and reconfigurable for different measurement needs. Epochs of both discrete voltage and current samples generated by the voltage-controlled current source are processed using a digital signal processing algorithms to generate admittance measurements. In addition to the admittance's magnitude and phase, pressure, electrocardiogram (EKG), and temperature (two channels) data are also acquired. The measurements are then wirelessly transmitted from the bio-impedance measurement system to a base station where data are processed and viewed graphically. The final system updates the admittance, pressure, EKG, and two temperature channels at 320 Hz, consumes less than 3 W, and has percent of measurement errors of 7 % and 2 % for capacitive and resistive measurements in the range of 100 pF to 10000 pF and 300  $\Omega$  to 1600  $\Omega$ , respectively. Instrument design, calibration, verification, and modeling are at the heart of this thesis. In the future, the instrument will be deployed for various bio-impedance measurements that require a high degree of linearity, precision, and a wide input range.

# Table of Contents

Table of Contents .....	xii
List of Figures .....	xiv
List of Tables.....	xvi
Chapter 1: Introduction .....	1
1.1 Motivation .....	1
1.2 Previous Generation Bio-impedance Measurement System.....	5
1.3 Next Generation Bio-impedance Measurement System.....	6
Chapter 2: Implementation.....	8
2.1 Admittance Theory.....	8
2.1.1 Parallel Model.....	8
2.1.2 Measuring Admittance.....	10
2.2 Design Strategy .....	12
2.3 Block Diagrams .....	13
2.4 Analog Hardware .....	15
2.4.1 Voltage, Current, EKG, Temperature and Pressure Channels.....	15
2.4.2 Power Supply Rails and References.....	16
2.4.3 Current Source and Measurement.....	17
2.4.4 Filters.....	19
2.4.5 Operational and Instrumentation Amplifiers.....	20
2.4.6 Passive Components.....	21
2.4.7 Pressure Sensor.....	22
2.4.8 Temperature Sensor.....	24
2.5 Digital and Mixed Signal Hardware.....	24
2.5.1 MCU.....	24
2.5.2 ADC .....	26
2.5.3 DAC.....	27
2.6 Firmware .....	29
2.7 Wireless Communication .....	30
2.8 Admittance Calibration .....	33

2.9 Thermocouple Calibration.....	35
2.10 Pressure Calibration.....	36
2.11 Breadboard Prototyping.....	38
2.12 PCB Assembly and Electrical Verification .....	38
Chapter 3: System Verification .....	40
3.1 Admittance RC Load Test.....	40
3.2 EKG Extraction .....	43
3.3 Noise.....	44
3.4 Wireless Channel Transmission Integrity.....	48
3.5 Slew Rate and Headroom .....	48
3.6 CMRR .....	51
3.7 Frequency Jitter .....	53
3.8 Power Consumption .....	54
Chapter 4: Conclusion .....	55
4.1 New Measurement System .....	55
4.2 Unresolved Issues.....	56
4.3 Future Direction .....	56
References .....	58

## List of Figures

Figure 1: Internal View of the Spring-loaded Device Used for the Housing of the Surface Probe, Equipped with Admittance, Pressure, and Temperature Sensors.....	5
Figure 2: External View of the Spring-loaded Device with Arrows Showing How the Signals Are Distributed. ....	7
Figure 3: Intra-ventricular Parallel Model [11-13].....	8
Figure 4: Myocardial Parallel RC Model. ....	10
Figure 5: Simplified Tetrapolar Configuration.....	12
Figure 6: System Block Diagram. ....	13
Figure 7: Wireless Measurement System Block Diagram.....	14
Figure 8: Voltage, Current, and EKG Channels.....	16
Figure 9: Temperature and Pressure Channels. ....	16
Figure 10: Current Source. ....	18
Figure 11: Differential Measurement Circuit. ....	18
Figure 12: First-order High Pass Filter with Voltage Scaling. ....	19
Figure 13: Second-order Sallen-Key Low Pass Filter. ....	20
Figure 14: Wheatstone-bridge Pressure Transducer (left) and R4 Internal Circuit (right).....	22
Figure 15: Resistance (k $\Omega$ ) vs Force (lb) Characteristic. ....	23
Figure 16: TM4C123 Microcontroller Architecture Overview [18] .....	24
Figure 17: Launchpad (red board) Used for Programming and Debugging the Target Microcontroller.....	25
Figure 18: DAC-ADC-Delay Measurement Architecture for a Single Cycle. ....	27
Figure 19: DAC Filtered Output Waveform.....	28
Figure 20: DAC Output Frequency Spectrum.....	28
Figure 21: DAC Output Waveform Shown for Several Admittance Samples. ....	29
Figure 22: Color-coded Firmware Architecture Depicted in Three Levels.....	30
Figure 23: Xbee Wireless Transceiver Modules with Xbee Explorer USB Adapters.....	30
Figure 24 Xbee Network Layers [21].....	32
Figure 25: Phase Offset Variability.....	34
Figure 26: Resistor Sweep Calibration Results. ....	34
Figure 27: Thermocouple Calibration Experimental Setup.....	35
Figure 28: Thermocouple Calibration Curve.....	36
Figure 29: Pressure Sensor System. ....	37
Figure 30: Pressure Calibration Curve. ....	37
Figure 31: Breadboard Prototype. ....	38
Figure 32: Board Assembly and Electrical Verification .....	39
Figure 33: Absolute and Percent of Measurement Errors in Terms of Resistive Error.....	41
Figure 34: Absolute and Percent Measurement Errors in Terms of Capacitive Error.....	41
Figure 35: Previous (left) and New (right) Capacitive Percent of Measurement Error.....	42

Figure 36: Previous (left) and New (right) Resistive Percent of Measurement Error. ....	42
Figure 37: Previous (left) and New (right) Capacitive Measurement Error. ....	42
Figure 38: Previous (left) and New (right) Resistive Measurement Error. ....	42
Figure 39: EKG and 20 kHz Admittance Signals.....	43
Figure 40: Extracted EKG Signal.....	43
Figure 41: Measured EKG Signal at 320 Hz.....	44
Figure 42: Noise at ADC0 Input. ....	44
Figure 43: Noise at ADC1 Input. ....	45
Figure 44: STD for R and C Measurements. ....	46
Figure 45: SNR Based on R Measurements. ....	46
Figure 46: SNR Based on C Measurements. ....	47
Figure 47: Measuring INA SR Using the Rising Edge of a 20 kHz Square Wave. ....	50
Figure 48: CMRR Measurement Setup for Common (top) and Differential (bottom) Modes.....	52
Figure 49: CMRR Frequency Sweep. ....	52

## List of Tables

Table 1: Data Package Composition .....	32
Table 2: Current Source Frequency Jitter Measurements. ....	54
Table 3: System Performance Summary. ....	55

# Chapter 1: Introduction

## 1.1 Motivation

It is estimated that over four million Americans, most over age sixty, experience some form of cardiac arrhythmias that require medical attention [1]. An arrhythmia is a disorder of the cardiac conduction system that is responsible for directing and regulating normal heart functions. Some risk factors that affect the cardiac conduction system are: heart disease, abnormal balance of electrolytes, changes in heart muscle, and injury to the heart [2]. There are many different variations of cardiac arrhythmia, and they are named and categorized based on three features including the rate, origin, and regularity [3]. Some examples include bradycardia, tachycardia, supraventricular tachycardia, and ventricular tachycardia. When the resting heart rate is less than 60 beats per minute (bpm) it is called bradycardia. In contrast, when the resting heart rate is greater than 100 bpm it is called tachycardia. Supraventricular and ventricular tachycardias refer to an arrhythmia that originates above and on the ventricle, respectively. One of the most common forms of supraventricular tachycardia is atrial fibrillation (AF). AF causes the atrium to beat rapidly (~240 bpm) such that it is unable to contract completely but rather it fibrillates. If left untreated, AF may lead to more serious complications, such as a stroke [3].

In a healthy heart, each heartbeat is set into motion by an electrical impulse that originates from the sinoatrial (SA) node, the heart's natural pacemaker. The SA node is located in the right atrium, near the superior vena cava. This physiological pacemaker exhibits a spontaneous depolarization that causes action potentials, resulting in automatic beating of the heart. From the SA node, the electrical impulse then rapidly spreads (0.8 to 1 m/s) to the adjacent myocardial cells of the left and right atria via the gap junctions between these cells.

Nevertheless, the impulse cannot be conducted directly from the atria to the ventricles because the myocardium of the atria and ventricles are electrically separated by the fibrous skeleton of the heart [4]. Thus, specialized conducting myocardial cells are required. These specialized cells constitute the atrial-ventricular (AV) node, bundle of His, bundle branches, and Purkinje fibers. Once the impulse has spread through the atria, it then passes to the AV node. The conduction slows down significantly when it passes into the AV nodes (0.03 to 0.005 m/s). From the AV node, the impulse continues through the bundle of His, the left and right bundle branches, and finally the Purkinje fibers within the ventricular walls. Following a brief AV delay (~0.1s), the conduction rate increases considerably in the bundle of His and reaches high speeds in the Purkinje fibers (5 m/s). Stimulation of Purkinje fibers causes the ventricles to simultaneously contract and eject blood into the pulmonary and systemic circulation. Any disruption to this synchronous operation may cause cardiac arrhythmia.

There are a number of disease mechanisms that can disrupt the normal electrical activity of the heart. Some diseases affect the electrical pathways which may slow down or even block the electrical impulse completely. Some regions of the heart, including areas around the SA node and the AV bundle, can potentially produce local pacemaker potentials [4]. Normally, these local pacemakers depolarize at a slower rate than that of the SA node. Thus, the SA node, by stimulating these potential pacemaker sites before they can stimulate themselves, prevents disorganized heart contraction. Now, if the conduction pathway is somehow blocked, the potential pacemaker sites will spontaneously generate their own action potentials and will function as abnormal pacemakers or ectopic foci. These ectopic foci affect the natural pacing rhythm of the heart, resulting in cardiac arrhythmia.

It is not unusual for people to experience an occasional, harmless arrhythmia; such as skipped, irregular, or racing heart beats. In fact, a healthy heart will either beat faster or slower throughout the day depending on the activity level to accommodate the body's changing need for oxygen. However, for some, cardiac arrhythmias may be a harbinger of serious or even life-threatening complications such as a stroke if left untreated [3]. One of the most common alternative treatment options for patients suffering from drug-resistant cardiac arrhythmia is catheter-based Radio Frequency (RF) cardiac ablation. The ablation catheter is used to deposit rapid, high doses of energy to the ectopic sites that aims to terminate the ectopic cells and restore normal heart rhythm [5]. RF ablation, delivered through the electrodes at the tip of the catheter, is caused by the electrical current that rapidly heats the target tissue leading to cell necrosis. Currently, the only available indicator of tissue viability that aids physicians during an ablation treatment is the intra-cardiac electrocardiogram (ICEKG). However, this practice presents the potential issue of mislabeling a treated ectopic tissue as necrosis while it is in fact stunned—a temporary outcome. In this particular scenario, the ICEKG signal would suggest superficial cell death, but, after several weeks, the ectopic cells will become active again, and the patient will have to undergo additional treatments. In addition to unreliable ICEKG feedback, physicians are unable to quantify the applied pressure at the tip. Consequently, the lack of physical feedback poses the serious risk of the physician perforating the heart septum during treatment. To rectify these challenges, the treatment process requires a method that can identify proper contact with the myocardium, indicate applied pressure, and distinguish between healthy, stunned, and scarred myocardial tissue.

A proposed method that has the potential to solve these issues is the Admittance-Ablation Catheter approach. This method exploits the capacitive nature of the myocardium trans-

membrane charge distribution. Previous studies have shown that there is a difference in impedance measurement between infarcted, normal, and stunned tissue [6, 7]. The hypothesis is that the thermal destruction of the ectopic cardiac cells via RF ablation will induce a significant change in the permittivity relative to healthy cardiac cells and will be detectable by the admittance method. This will allow the physicians to make the appropriate decision with regard to the viability of the targeted tissue in real time. It is important to note that the ICEKG will not be excluded in this modality. In other words, admittance, used as a measure of cell viability, will be added to the existing therapy procedure. The admittance measurement and ICEKG can be measured simultaneously since they can be separated in the frequency domain preferably via analog filters. As a result, physicians will have the luxury of two feedback modalities. This solution requires a novel tetra-polar concentric-ring-electrode catheter tip configuration designed for two modes: ablation and admittance sensing. In addition, to prevent perforating the heart septum, the catheter will be equipped with a contact pressure sensor for physical feedback.

The ultimate goal is to design a bio-impedance measurement system using the tetra-polar concentric-ring-electrode catheter architecture with an optical pressure sensor positioned at the center of the tip. However, for the sake of demonstrating the feasibility of measuring permittivity changes in real-time during RF ablation, it is wiser to implement the design on a large-scale prototype using a spring-loaded architecture for a relatively shorter research and development time and at a lower cost, Figure 1. In general, the feasibility of measuring permittivity using this larger scale prototype will ultimately dictate the implementation of the later-stage catheter-based design. This large-scale prototype design is described in the next section.

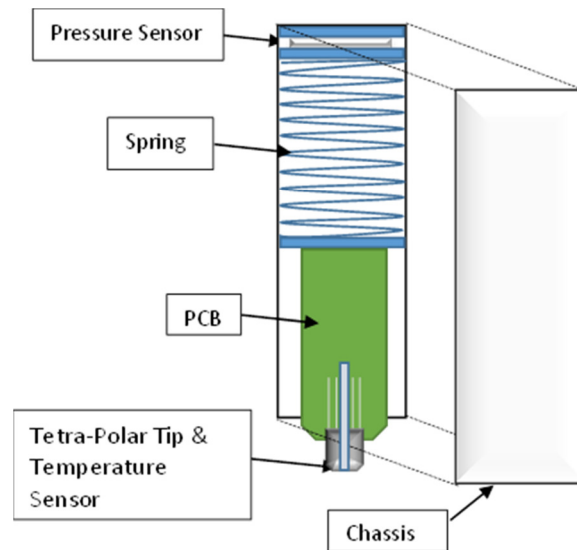


Figure 1: Internal View of the Spring-loaded Device Used for the Housing of the Surface Probe, Equipped with Admittance, Pressure, and Temperature Sensors.

## 1.2 Previous Generation Bio-impedance Measurement System

One of the specific aims from the preliminary cardiac ablation studies was to evaluate the feasibility of monitoring the essential electrical properties of heart, such as permittivity and conductivity, in real time. These experiments were monitored via a pre-existing bio-impedance monitoring instrument designed by Erik Larson [8, 9]. The outcome from the initial studies was inconclusive due to the limited measurement range of the device. In other words, the instrument was used beyond its intended measurement range. One of the immediate consequences was a faulty permittivity read-out that was initially thought to be a temperature dependent issue, but later was verified to be a load-dependent issue. The root cause of the load dependency was later attributed to the linearity of the instrument. The linearity of the instrument is a crucial specification that determines the practical measurement range. In addition, preliminary studies have identified the need that the device can ensure consistent measurements over time. The issue of physical contact inconsistency was raised following various observations of motion artifacts

occurring during the preliminary *in vivo* experiments. Physical contact pressure variability from experiment to experiment is a significant source of uncertainty on admittance measurements. On a positive note, the preliminary studies did provide many valuable insights as to the new instrumentation requirements needed for a reliable admittance measurement during cardiac ablation.

### **1.3 Next Generation Bio-impedance Measurement System**

The previous challenges encountered have motivated the next generation of bio-impedance instruments that will be specifically optimized for performance, without constraints of power or size. However, it will be flexible enough to be reconfigured for various measurement ranges. The new instrument will be completely battery-powered for optimal noise immunity, portability, and its bio-impedance measurement range will be extended appropriately. The resistive and capacitive load range requirements are: 300-1600  $\Omega$  and 100-10000 pF. For cardiac ablation studies, it is important that the capacitive and resistive relative measurement errors are within 5% and 2%, respectively. In addition, the new device will have means of monitoring the intra-cardiac electrocardiogram, contact pressure using a spring-loaded device, and temperature using an insulated K-type thermocouple, Figure 2. To measure the dynamic bio-impedance signal an oversampling factor of fifty is used. Since the maximum heart rate of large animals is 3.7 Hz [9], the minimum sampling rate needed is 183 S/s. The system will be configured so that the overall sampling rate is 200 S/s. In other words, admittance magnitude, admittance phase, temperature, pressure, and EKG data will be updated at 200 times per second or more. One of the major architectural changes in this new generation is the inclusion of a current sensing channel. Previously, only voltage sensing was employed to measure both amplitude and phase variations and it was assumed to be adequate. However, measurements

showed that the constant current source was not constant over the range of loads, causing a load-dependent error. The result has motivated the necessity of a current sensing channel that will serve as a real-time reference. In the following sections, the instrument design, calibration, verification, and modeling will be discussed in detail.

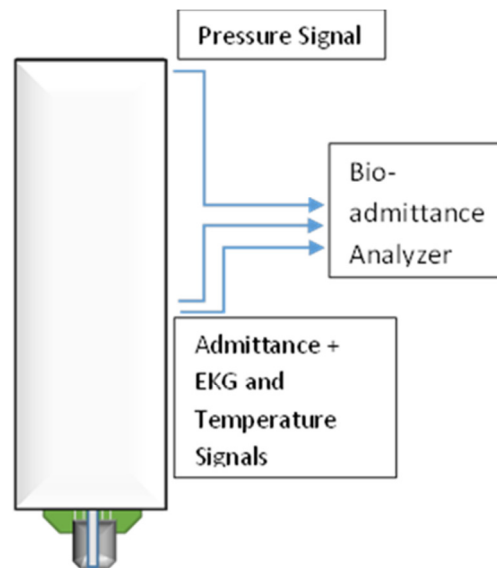


Figure 2: External View of the Spring-loaded Device with Arrows Showing How the Signals Are Distributed.

## Chapter 2: Implementation

### 2.1 Admittance Theory

#### 2.1.1 Parallel Model

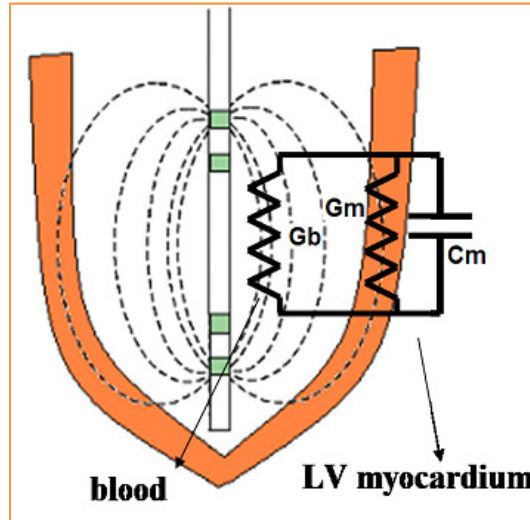


Figure 3: Intra-ventricular Parallel Model [11-13].

It is useful to approximate biological systems in terms of circuit models. One of the circuit models that is used to model the electrical characteristics of the heart is the parallel RC model, Figure 3, [11-13]. Note that the figure depicts an intra-ventricular parallel model that includes the blood pool conductance contribution. For surface myocardium measurements, the stimulating current field is localized and the blood component can be neglected.

This section will introduce some of the basic measurement terminologies. Sometimes it is more convenient to describe parallel circuits in terms of admittance in lieu of impedance. Recall that admittance  $\mathbf{Y}$ , the inverse of impedance  $\mathbf{Z}$ , is a complex value measured in Siemens.  $\mathbf{Y}$  is composed of both real and imaginary components (2.1) [14].

$$\mathbf{Y} = \frac{1}{\mathbf{Z}} = G + jB. \quad (2.1)$$

The real component of admittance is referred to as the conductance  $G$  and the imaginary component of admittance is referred to as the susceptance  $B$ . To capture both the magnitude and phase information a polar representation of admittance is often used, equation (2.2).

$$\mathbf{Y} = |\mathbf{Y}|e^{j\angle\mathbf{Y}} \quad (2.2)$$

$$|\mathbf{Y}| = \sqrt{G^2 + B^2} \quad (2.3)$$

$$\angle\mathbf{Y} = \text{atan}\left(\frac{B}{G}\right) \quad (2.4)$$

$|\mathbf{Y}|$  from equation (2.3) and  $\angle\mathbf{Y}$  from equation (2.4) represent the magnitude and phase of the complex admittance  $\mathbf{Y}$ , respectively. Now given  $\mathbf{Y}$ , the real and imaginary admittance components can be calculated using equations (2.5) and (2.6), respectively.

$$\text{Real}(\mathbf{Y}) = G = |\mathbf{Y}|\cos(\angle\mathbf{Y}) \quad (2.5)$$

$$\text{Imag}(\mathbf{Y}) = B = |\mathbf{Y}|\sin(\angle\mathbf{Y}) \quad (2.6)$$

For a simple parallel RC circuit, Figure 4, the complex impedance  $\mathbf{Z}$ , the real part of  $\mathbf{Z}$ , and the imaginary part of  $\mathbf{Z}$  are given by the following equations:

$$\mathbf{Z} = \frac{R1}{1+j\omega R1C1} \quad (2.7)$$

$$\text{Real}(\mathbf{Z}) = \frac{R1}{1+\omega^2 R1^2 C1^2} \quad (2.8)$$

$$\text{Imag}(\mathbf{Z}) = -\frac{\omega R1^2 C1}{1+\omega^2 R1^2 C1^2} \quad (2.9)$$

where  $\omega$  is the radial frequency. Now, the admittance  $\mathbf{Y}$  is given by the following equation:

$$\mathbf{Y} = \frac{1}{\mathbf{Z}} = \frac{1+j\omega R_1 C_1}{R_1} = \frac{1}{R_1} + j\omega C_1 \quad (2.10)$$

where, in this case,  $G = \frac{1}{R_1}$  and  $B = \omega C_1$ .

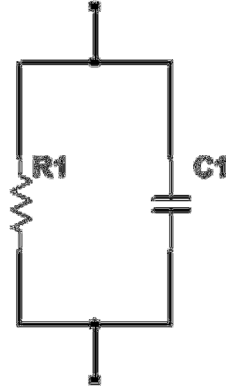


Figure 4: Myocardial Parallel RC Model.

### 2.1.2 Measuring Admittance

To measure admittance, a stimulating current source is used. To avoid measuring the electrode series impedances,  $Z_1$  and  $Z_4$ , a tetrapolar electrode configuration can be used, Figure 5. Note that the impedances  $Z_1$ ,  $Z_2$ ,  $Z_3$ , and  $Z_4$  are the complex electrode-electrolyte impedances. The “e” labels represent the electrodes: e1 and e4 are the current source electrodes and e2 and e3 are the sensing electrodes. Assuming negligible current flowing into the instrumentation amplifier, the voltage drop across  $Z_{LOAD}$  can be measured. From the right-hand side of Ampere’s Law, the total current flowing through a load generates a potential difference that is measureable:

$$\vec{\mathbf{J}} = (\sigma + j\omega\epsilon)\vec{\mathbf{E}} \quad (2.11)$$

where  $\sigma$  (S/m) and  $\epsilon$  (F/m) are the electrical conductivity and permittivity parameters representing the unique electrical properties of the target tissue.  $\vec{\mathbf{J}}$  ( $A/m^2$ ) is the total current density vector (including drift

and displacement current densities) and  $\vec{E}$  (V/m) is the electric field vector. Now,  $\mathbf{Y}$  is simply the ratio of complex current to complex voltage:

$$\mathbf{Y} = \frac{|\mathbf{I}|e^{j\angle\mathbf{I}}}{|\mathbf{V}|e^{j\angle\mathbf{V}}} \quad (2.12)$$

Earlier, the admittance's magnitude and phase were described in terms of G and B. Now, the admittance  $|\mathbf{Y}|$  and  $\angle\mathbf{Y}$  and will be described in terms of measured current  $\mathbf{I}$  and voltage  $\mathbf{V}$  (complex values) using equations (2.13) and (2.14), respectively.

$$|\mathbf{Y}| = \frac{|\mathbf{I}|}{|\mathbf{V}|} \quad (2.13)$$

$$\angle\mathbf{Y} = \angle\mathbf{I} - \angle\mathbf{V} \quad (2.14)$$

To calculate R and C once  $\mathbf{Y}$  is determined:

$$R = \frac{1}{G} = \frac{1}{\text{Real}(\mathbf{Y})} = \frac{1}{|\mathbf{Y}|\text{Cos}(\angle\mathbf{Y})} \quad (2.15)$$

$$C = \frac{\text{Imag}(\mathbf{Y})}{\omega} = \frac{|\mathbf{Y}|\text{Sin}(\angle\mathbf{Y})}{\omega} \quad (2.16)$$

Now, C is composed of both the measuring probe's capacitance and the tissue's capacitance. Saline calibration can be done to measure the probe's contribution prior to measuring tissue capacitance [15].

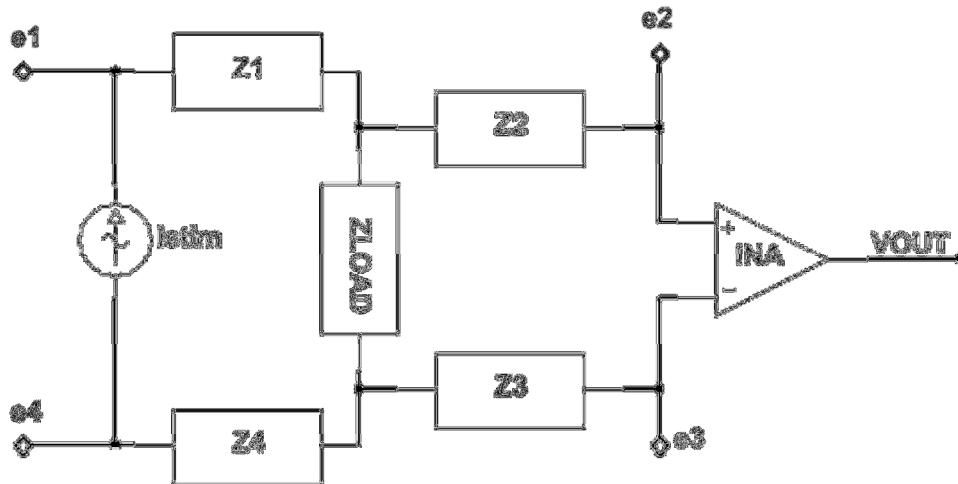


Figure 5: Simplified Tetrapolar Configuration.

## 2.2 Design Strategy

Having a solid design strategy is important to minimize research and development time and thus cost. In general, a good design strategy enhances productivity over the time. This is especially true for high-risk designs under budget constraints. High-risk designs includes designs where novel architectures are being explored. One of the basic design strategies include having a modular design with build-in redundancy. It is always a good idea to have a few backup plans. This will maximize the chances of a build success for the first prototype. Having design calculations and application notes well documented is necessary for reproducibility. A common practice used in industry is to document all calculations using software such as Mathcad or similar tools. Using software, a design flow is facilitated and thus the design process is more transparent for various design or verification cycles. In addition, having an organized design flow ensure a more thorough design process that increases the probability of catching design flaws.

## 2.3 Block Diagrams

The system is composed of three primary blocks: the sensors, the wireless measurement system, and the computer with a wireless receiver, Figure 6. The sensors include a tetra-polar surface probe, a piezoresistive pressure sensor, and two K-type thermocouple temperature sensors. The surface probe allows for differential voltage measurements which admittance and EKG signals are extracted. The wireless measurement system includes multiple analog stages for signal conditioning, a digital to analog converter (DAC), a 32-bit microcontroller (MCU) with two physical successive approximation register (SAR) analog-to-digital converters (ADCs) for data acquisition, and an Xbee for wireless transmission, Figure 7. The two physical ADCs allow for simultaneous measurements of the voltage and current channels to avoid phase offset in the measurement itself. A more in depth discussion is in the ADC section. Lastly, the receiver side includes an XBee and a computer for data recording and display.



Figure 6: System Block Diagram.

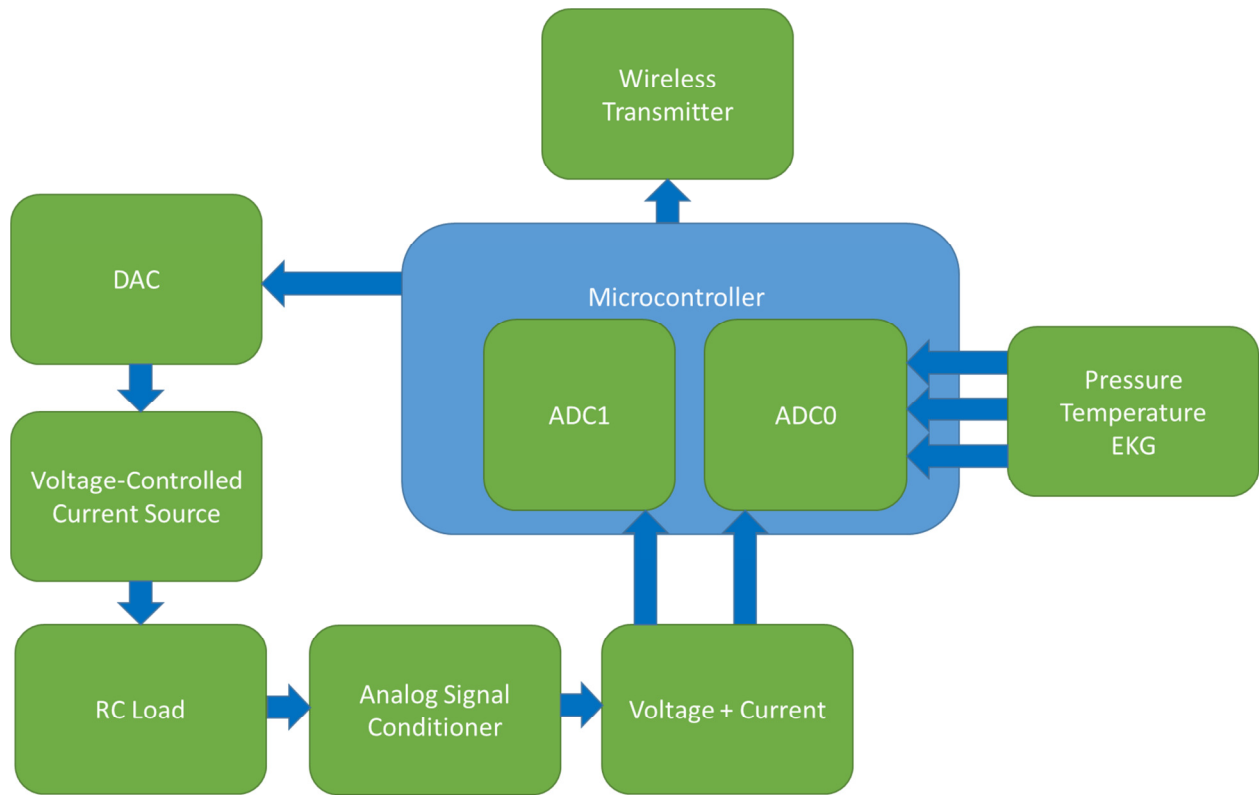


Figure 7: Wireless Measurement System Block Diagram.

## 2.4 Analog Hardware

### 2.4.1 Voltage, Current, EKG, Temperature and Pressure Channels

An architecture overview of the voltage, current, EKG, temperature, and pressure channels are shown in Figures 8 and 9. Note, only one of the two temperature channels is shown in Figure 9, since they are identical copies. The current channel has a small fixed load for sensing current and the instrumentation amplifier (INA) gain was set to 400 V/V to maximize common mode rejection. As for the wide-input-range voltage channel, the INA gain was set to 40 V/V to prevent clipping. This is a compromise between common mode rejection ratio (CMRR) and input range because CMRR increases with INA gain and gain is limited by the maximum input load. Lastly, the EKG was filtered from the voltage channel using a buffered low-pass stage with a cut-off at 500 Hz. In theory, an EKG bandwidth of 100 Hz is adequate. The 500 Hz EKG bandwidth allows more flexibility for digital filtering later on.

The temperature channel has an overall gain of 500 and its cut-off was set to 500 Hz. Assume the temperature slew rate is 10 °C/s, if temperature is sampled every 2 ms, then the temperature will rise 0.02 °C each sample. From the initial studies, a typical temperature slew rate of 1 °C/s was observed during cardiac ablation. Thus a measurement bandwidth of 500 Hz is adequate. The 500 Hz sampling also allows for flexible digital filtering in the software stage. The pressure sensor is placed inside a Wheatstone bridge for amplification prior to the INA stage that gives it additional gain and common mode rejection. Since the maximum expected heart rate for large animals is 3.7 Hz the cut-off was set to 5 Hz. A more in depth discussion are discussed in subsequent sections.

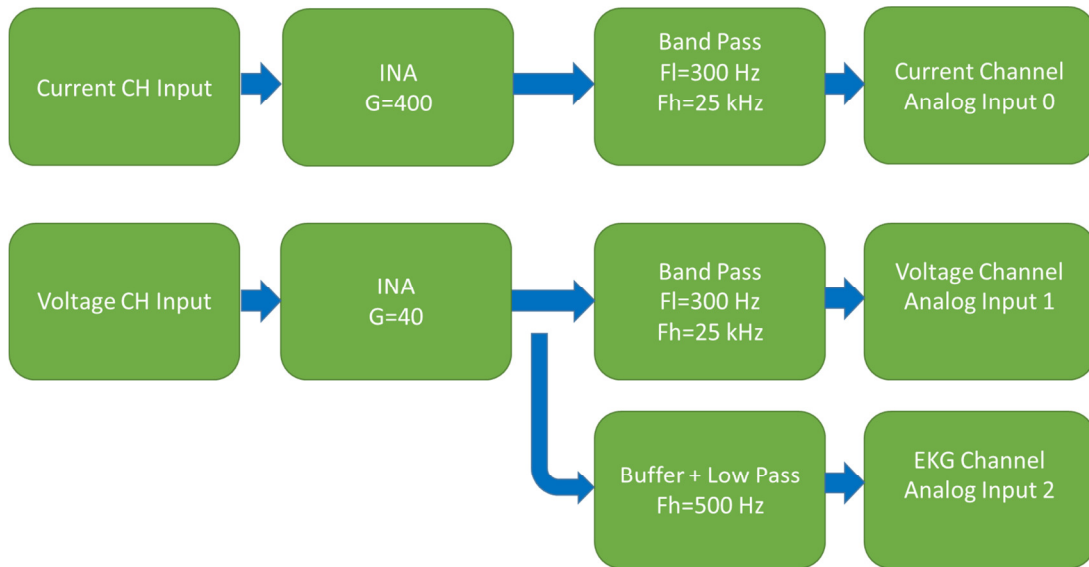


Figure 8: Voltage, Current, and EKG Channels.



Figure 9: Temperature and Pressure Channels.

## 2.4.2 Power Supply Rails and References

The system is powered with four Tenergy Li-Ion 18650 7.4V (8.4V maximum when fully charged) 2200mAh rechargeable battery modules. A clean DC power supply allows for acceptable analog performance and with rechargeable Li-ion batteries it is possible to achieve thirteen hours per usage. When connected in series they are capable of providing supply

voltages of  $\pm 14.8\text{V}$  and  $\pm 7.4\text{V}$ . The center-tap of the four modules provides the ground (GND) reference for the system. Each module has internal voltage and current protections and will automatically shut off when its voltage drops below 6 V or when its discharge current is higher than 4.4 A. The  $\pm 14.8\text{ V}$  and  $+7.4\text{ V}$  are ultimately combined with four linear regulators (for low noise) to provide the  $\pm 12\text{V}$ ,  $+5\text{V}$ ,  $+3.6\text{V}$  regulated supply rails required. In addition, an integrated circuit (IC) is used to provide a  $+1.8\text{V}$  reference necessary to bias the direct current (DC) level of the voltage and current channels. This allows for a full-input swing of 3.6 V into the single-ended unipolar SAR ADCs.

### 2.4.3 Current Source and Measurement

A voltage-controlled current source was used to stimulate the target load, Figure 10.  $I_{\text{stim}}$  is the current used to stimulate the load. The current source transfer function is simply:

$$I_{\text{stim}} = \frac{V_{\text{in}}}{R_s} \quad (2.17)$$

where  $V_{\text{IN}}$  is the properly filtered and scaled DAC output waveform and  $R_s$  is the set resistor (sets the current). The voltage drop across  $Z_{\text{load}}$  serves as a raw input into the voltage channel and the voltage drop across the  $R_{\text{sense}}$  resistor serves as a raw input to the current channel. Only one capacitor is needed to prevent DC current from flowing into the load assuming the load is isolated from system reference GND. DC current is notorious for corroding electrodes and should be generally avoided in biomedical measurements.

A differential measurement circuit is used to sense the voltage drop across the load for the admittance voltage channel, Figure 11. The same circuit can be applied for sensing the voltage across the  $R_{\text{sense}}$  resistor for the admittance current channel. Note, a high-pass filter (HPF) is used for blocking DC bias current from entering the tissue. The HPF is also used to

prevent DC drift emanating from the electrodes half-cell potential. Small variation of the signal conditioner block allows the EKG signal to be extracted from the admittance voltage channel.

This is accomplished with a voltage buffer and a low-pass filter.

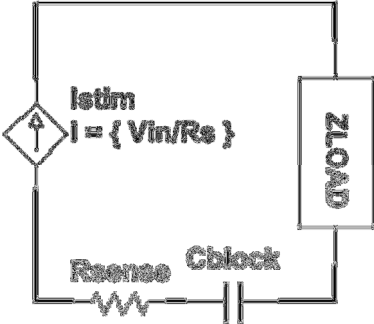


Figure 10: Current Source.

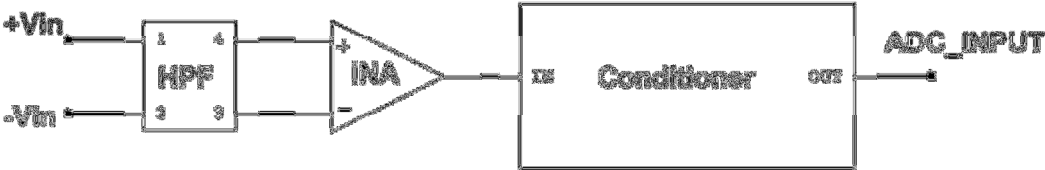


Figure 11: Differential Measurement Circuit.

## 2.4.4 Filters

There are two basic filters used in the conditioner following the INA stage. The first one is a first-order high-pass filter with a buffered output stage, Figure 12. Its transfer function and corner frequency are described in equations (2.18) and (2.19), respectively. The filter is a basic passive high-pass filter with a divider built-in for scaling the output voltage  $V_{out}$  to the ADC range (0 to 3.6 V). The high-pass corner is set to 230 Hz, which is high enough for filtering low frequencies such as EKG and low enough not to affect the 20 kHz admittance signal. The second filter is the Sallen-Key filter, Figure 13. The Sallen-Key is configured as a second-order low-pass filter and its transfer function, quality factor  $Q$ , and corner frequency are described in equations (2.20), (2.21), and (2.22), respectively [16]. The low-pass corners used for the current, voltage, EKG, pressure, and temperature are 25 kHz, 25 kHz, 500 Hz, 5 Hz, and 500 Hz, respectively. Note, the design is simplified if there are similar corner frequencies. The  $Q$  for all filters is designed to be  $\sim 0.7$  for maximum stability and optimal frequency response (in terms of flatness).

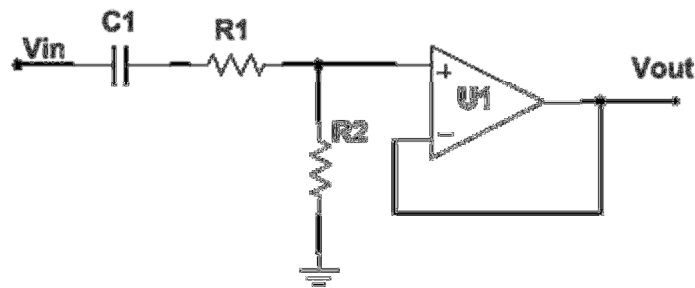


Figure 12: First-order High Pass Filter with Voltage Scaling.

$$H(s) = \frac{R2}{(R1+R2)} * \frac{s}{s+\omega_o} \quad (2.18)$$

$$f_o = \frac{\omega_o}{2\pi} = \frac{1}{2\pi(R1+R2)C1} \quad (2.19)$$

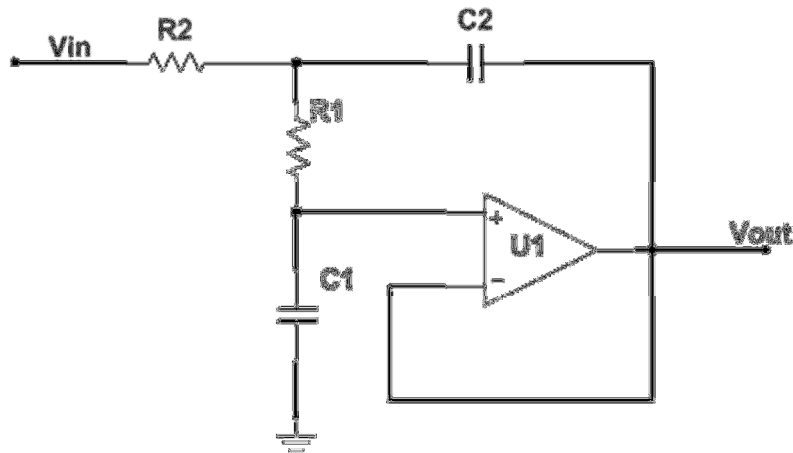


Figure 13: Second-order Sallen-Key Low Pass Filter.

$$H(s) = \frac{\omega_o^2}{s^2 + s\frac{\omega_o}{Q} + \omega_o^2} \quad (2.20)$$

$$Q = \omega_o \frac{R_1 R_2 C_1}{R_1 + R_2} \quad (2.21)$$

$$f_o = \frac{\omega_o}{2\pi} = \frac{1}{2\pi\sqrt{R_1 R_2 C_1 C_2}} \quad (2.22)$$

## 2.4.5 Operational and Instrumentation Amplifiers

For the current source, a low offset 75  $\mu\text{V}$ , low offset drift 0.6  $\mu\text{V}/^\circ\text{C}$  maximum, and low noise 2.8  $\text{nV}/\sqrt{\text{Hz}}$  operational amplifier (op-amp) was used to maximize stability. Since the current source output voltage swing is relatively small a slew rate of 2.5  $\text{V}/\mu\text{s}$  is adequate. The current source's op-amp has a gain bandwidth product (GBWP) of 10 MHz, which is more than enough for this application.

For the INA, a fast slew rate was needed to satisfy the wide output voltage swing of approximately  $\pm 10\text{ V}$  at 20 kHz. The INA chosen has a nominal slew rate of 4  $\text{V}/\mu\text{s}$ . This is

adequate given the maximum slew rate required for the voltage channel is  $1600\Omega * 140\mu\text{A} * 40 * 2\pi * 20\text{kHz} = 1.1 \text{ V}/\mu\text{S}$  and the maximum slew rate required for the current channel is  $200\Omega * 140\mu\text{A} * 400 * 2\pi * 20\text{kHz} = 1.4 \text{ V}/\mu\text{S}$ . Note that the INA has a nominal GBWP of 20 MHz so at a gain of 400 the  $f_{3\text{db}}$  is 50 kHz. Thus the INA pole will have some attenuation effect on the output voltage of the current channel. Some of the most important features include a high CMRR at 20 kHz and high input impedances for both the differential and common modes. The datasheet boasts CMRRs from 60 dB to 80 dB for gains of 10 and 100, respectively. In addition, the common and differential input impedances are  $10^{10} \Omega || 2 \text{ pF}$  and  $10^{11} \Omega || 9 \text{ pF}$ , respectively. Nevertheless, the required high-pass filter stage (to block DC bias current) before the INA stage will ultimately degrade the INA rated performance.

For the low-pass filters, high performance audio op-amps with low noise  $6 \text{ nV}/\sqrt{\text{Hz}}$ , low total harmonic distortion (THD), and fast settling time (600 ns to 0.01%) were used to maximize low-pass performance. The minimum slew rate of these op-amps is  $40 \text{ V}/\mu\text{S}$ . Filter resistors in the range of tens of  $\text{k}\Omega$  were used to minimize  $4\text{kTR}$  noise and unnecessary power consumption.

## 2.4.6 Passive Components

To minimize temperature-dependent drifts the filter ceramic capacitors chosen were either NPO or COG rated and the thin-film resistors chosen have a temperature coefficient of  $100 \text{ ppm}/^\circ\text{C}$ . The thin-film resistor (Susumu) and ceramic capacitor (Kelmet) tolerances were 1% and 5%, respectively. However, in cases where component matching is crucial like at the INA input stage, resistor and capacitor tolerances were at least 0.1% and 1%, respectively.

## 2.4.7 Pressure Sensor

A Wheatstone bridge is used to detect changes in applied force on the piezoresistive sensor, left panel of Figure 14. The piezoresistive sensor is normally an open-circuit unless an external force is applied, Figure 15. Thus, the piezoresistive sensor needs a shunt resistor to lower its nominal resistance in order to keep the bridge's output from saturating. Saturating the output will cause the subsequent INA gain stage to rail to  $-12\text{ V}$ . Note that the INA is powered off the  $\pm 12\text{ V}$  rails since it is not a rail-to-rail INA. As the result, a resistor is connected in series with the piezoresistive sensor to limit the maximum output voltage of the Wheatstone bridge. Overall, the shunt and series resistors limit the output voltage of the INA from 0 to 3.6 V, which is the ADC input range, right panel of Figure 14.

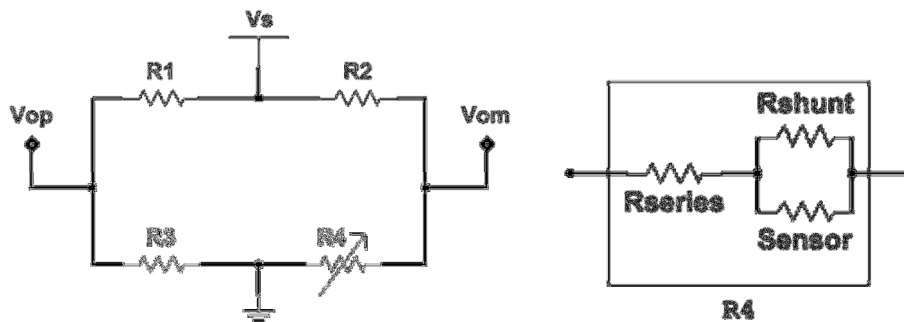


Figure 14 Wheatstone-bridge Pressure Transducer (left) and  $R_4$  Internal Circuit (right).

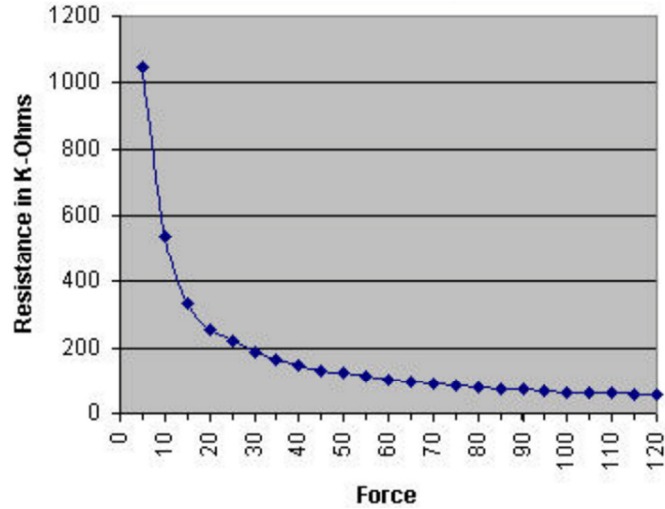


Figure 15: Resistance (kΩ) vs Force (lb) Characteristic.

Assuming the four legs of the bridge have equal nominal resistance ( $R_1=R_2=R_3=R_4=R$ ) and the bridge is balanced the output voltage is:

$$V_o = V_{op} - V_{om} = V_s \left( \frac{1}{2} - \frac{R_4}{R_4+R} \right) \quad (2.23)$$

where the output voltage  $V_o$  is the difference between the positive output  $V_{op}$  and the negative output  $V_{om}$ .  $V_s$  is the DC bias voltage,  $R$  is the nominal resistance of each of the four legs, and  $R_4$  is the effective sensor resistance after resistor padding.

The sensitivity of  $V_o$  with respect to the piezoresistive sensor  $R_4$  is

$$\frac{\partial V_o}{\partial R_4} = -V_s \left[ \frac{R}{(R_4+R)^2} \right] \quad (2.24)$$

where  $R_4$  includes the piezoresistive sensor resistance with the shunt and series padding resistors. The minimum and maximum  $R_4$  resistance after padding are the series padding resistor's resistance and  $R$ , respectively.

## 2.4.8 Temperature Sensor

Dissimilar metals forming a junction generate a voltage differential proportional to the junction temperature; the principle of a thermocouple. One of the most common types of thermocouples is the K-type. The K-type thermocouple is an inexpensive general purpose temperature sensor made from fusing chormel and alumel alloys—creating a junction. The sensor has a sensitivity of approximately  $41 \mu\text{V}/^\circ\text{C}$  near body temperature [17]. To interface with the thermocouple, a dedicated thermocouple instrumentation amplifier with an internal cold reference junction is used so that the overall sensitivity is increased to  $5 \text{ mV}/^\circ\text{C}$ . The amplifier is rated for a measurement range from  $20^\circ\text{C}$  to  $90^\circ\text{C}$ . Additional gain and filtering stages are added subsequently to set the final temperature channel output from 0 to 3.6 V.

## 2.5 Digital and Mixed Signal Hardware

### 2.5.1 MCU

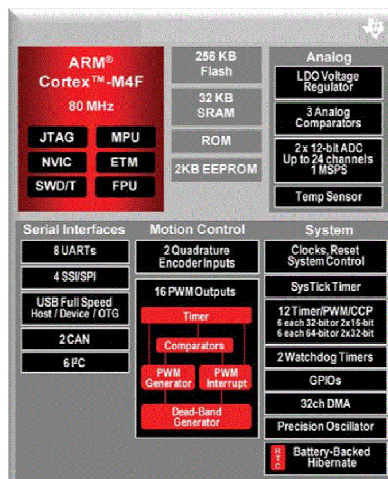


Figure 16: TM4C123 Microcontroller Architecture Overview [18]

The Tiva™ C Series TM4C123 is an advanced 32-bit microcontroller from Texas Instruments (TI), Figure 16. It has the following set of on-chip memory and features: 256 KB of flash, 32KB of single-cycle SRAM, 2KB of EEPROM, single precision floating point unit, up to 80 MHz of system clock frequency, two 12-bit SAR ADCs, and an internal ROM preloaded with TivaWare™ Peripheral Driver Library [18]. With the TivaWare Peripheral Driver Library the software development time is drastically reduced and allows the designer to focus more on system-level designs. To program and debug the target microcontroller a Tiva™ C Series LaunchPad evaluation board is used, Figure 17. Only five JTAG pins are needed to program the target microcontrollers: TDI, TDO, TMS, TCK, and GND [19]. Some additional advantages of using the Tiva™ C Series LaunchPad are that it allows for a full, unlimited license to the TI Code Composer Studio™ Integrated Development Environment and it has a large community for support.

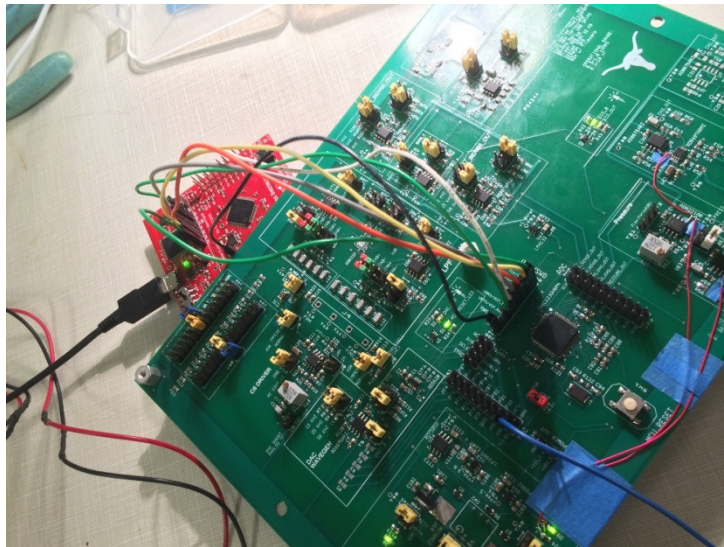


Figure 17: Launchpad (red board) Used for Programming and Debugging the Target Microcontroller.

## 2.5.2 ADC

One of the TM4C123 microcontroller's most important features is having two 1-MS/s SAR ADCs that allow simultaneous sampling. The SAR ADC implements a synchronous binary search algorithm and thus each 12-bit sample has a fixed sampling time. For the new admittance measurement architecture, both the voltage and current channels must be sampled at the same time instance to minimize phase offset caused by sampling. This is accomplished via delaying ADC0 with ADC\_TRIGGER\_WAIT and then performing a global ADC trigger with ADC\_TRIGGER\_SIGNAL to start ADC conversion for both ADC0 and ADC1:

```
ADCProcessorTrigger(ADC0_BASE, sequenceNum3|ADC_TRIGGER_WAIT);  
  
ADCProcessorTrigger(ADC1_BASE, sequenceNum3|ADC_TRIGGER_SIGNAL);
```

The two ADCs share a total of twelve analog input pins that are configured accordingly by programming the sampling sequencer. There are four programmable sampling sequencers inside the TM4C123 and only two sequencers are needed for the measurement system: sequence one and sequence three. Sequence 1 has a FIFO depth of four 32-bit words and is used for sampling temperature, pressure, and EKG channels. In particular, analog CH2, CH3, CH4, and CH5 are configured for the temperature 1, temperature 2, pressure, and EKG channels, respectively.

```
ADCSequenceConfigure(ADC0_BASE, sequenceNum1, ADC_TRIGGER_PROCESSOR, 0);  
ADCSequenceStepConfigure(ADC0_BASE, sequenceNum1, 0, ADC_CTL_CH2); //T1  
ADCSequenceStepConfigure(ADC0_BASE, sequenceNum1, 1, ADC_CTL_CH3); //T2  
ADCSequenceStepConfigure(ADC0_BASE, sequenceNum1, 2, ADC_CTL_CH4); //P  
ADCSequenceStepConfigure(ADC0_BASE, sequenceNum1, 3, ADC_CTL_CH5|ADC_CTL_IE|ADC_CTL_END); //EKG
```

Sequence 3 has a FIFO depth of one 32-bit word and is used for admittance current and voltage channels. In particular, analog inputs CH0 and CH1 are configured for the current and voltage channels:

```
ADCSequenceConfigure (ADC0_BASE, sequenceNum3, ADC_TRIGGER_PROCESSOR, 0);
ADCSequenceConfigure (ADC1_BASE, sequenceNum3, ADC_TRIGGER_PROCESSOR, 0);
ADCSequenceStepConfigure(ADC0_BASE, sequenceNum3, 0, ADC_CTL_CH0|ADC_CTL_IE|ADC_CTL_END);
ADCSequenceStepConfigure(ADC1_BASE, sequenceNum3, 0, ADC_CTL_CH1|ADC_CTL_IE|ADC_CTL_END);
```

For admittance measurements, the ADCs are configured to operate at a multiple of 20 kHz. Overall, the system was able to update admittance, temperature, pressure, and EKG samples at 320 Hz.

### 2.5.3 DAC



Figure 18: DAC-ADC-Delay Measurement Architecture for a Single Cycle.

Coherent and deterministic sampling is achieved with the DAC-ADC-Delay sequential architecture, Figure 18. An n-bit DAC is used to generate the sinusoidal waveform that controls the current source in the subsequent stage. The ADC-DAC-Delay architecture is similar to previous instruments [10, 15].

The raw DAC output is low-pass filtered with a second-order Sallen-Key filter. The filtered waveform is shown in Figure 19. A 10000-element, windowed DFT of the filtered DAC output shows a noise floor of -80 dBFS and thus the SNR is approximately 43 dB (SNR=80-

$10\log_{10}[10^4/2]$ ), Figure 20. The spectrum shows measurable 7<sup>th</sup> (-44.8 dBFS) and 9<sup>th</sup> (-52.0 dBFS) harmonics at 140 kHz and 180 kHz, respectively. The THD is calculated to be approximately -44 dB. A scaled-down version of this filtered DAC sinusoidal is the waveform that controls the 100  $\mu$ Arms current source. In the grander scheme of things, the system transmits all of the channel data at a rate of 320 Hz, Figure 21. While the DAC is off, the auxiliary measurements, signal processing, and data transmission occur.

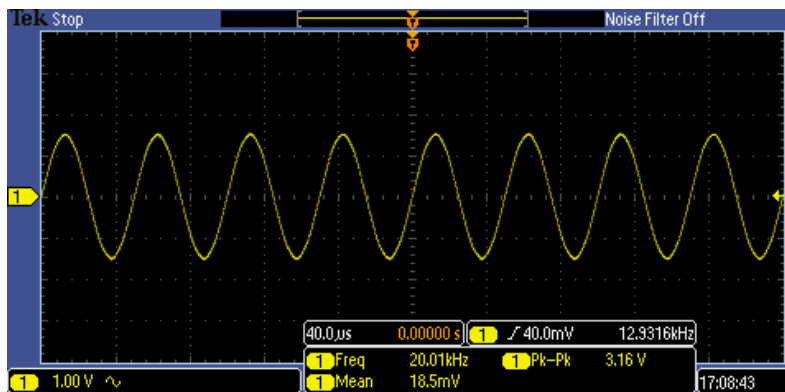


Figure 19: DAC Filtered Output Waveform.

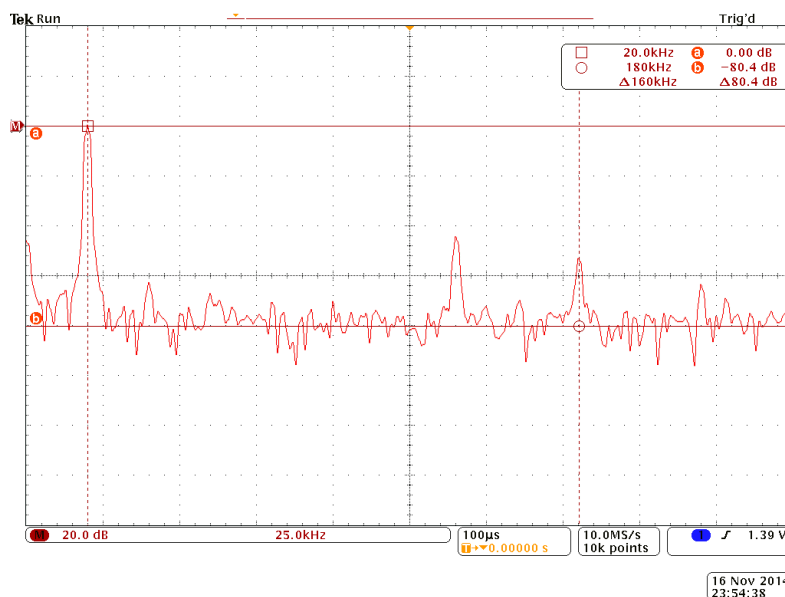


Figure 20: DAC Output Frequency Spectrum.

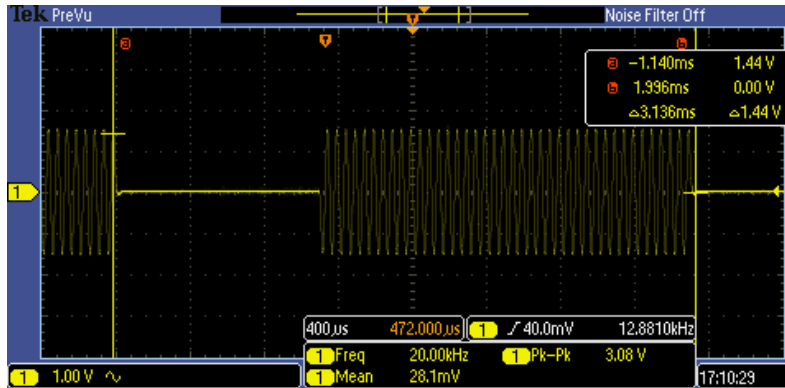


Figure 21: DAC Output Waveform Shown for Several Admittance Samples.

## 2.6 Firmware

The firmware code is composed of three distinct layers, Figure 22. Note that the figure is color-coded. At the lowest level the DAC outputs digital codes resembling a sine-wave. Again, the output code is optimized to minimize sine-wave distortion. Between the DAC outputs, both ADC0 and ADC1 with similar sampling sequences but different analog input channel configurations are simultaneously triggered for sampling. Next, a brief system delay is introduced to achieve the desired sinusoidal frequency of 20 kHz. The frequency is verified with an oscilloscope measurement to achieve a 20 kHz sinusoid. This ADC-DAC-Delay pattern is repeated, as seen in the middle layer of Figure 22. Using the data epoch stored in the previous step, admittance is then calculated using the complex voltage and current values from the DFT results. Following the DFT operations, ADC0 is triggered again but with a second sampling sequence that include consecutive measurements of EKG, pressure, and temperature. The last step in the middle layer of Figure 22 is the data transmission via an XBee transceiver. The transmission protocol is a simple UART protocol. A unique termination sequence is added in the transmission. This termination sequence is important for data synchronization between

transmissions to ensure proper data package handling on the receiver. The top layer of Figure 22 shows how this operation is basically repeated in an infinite loop.

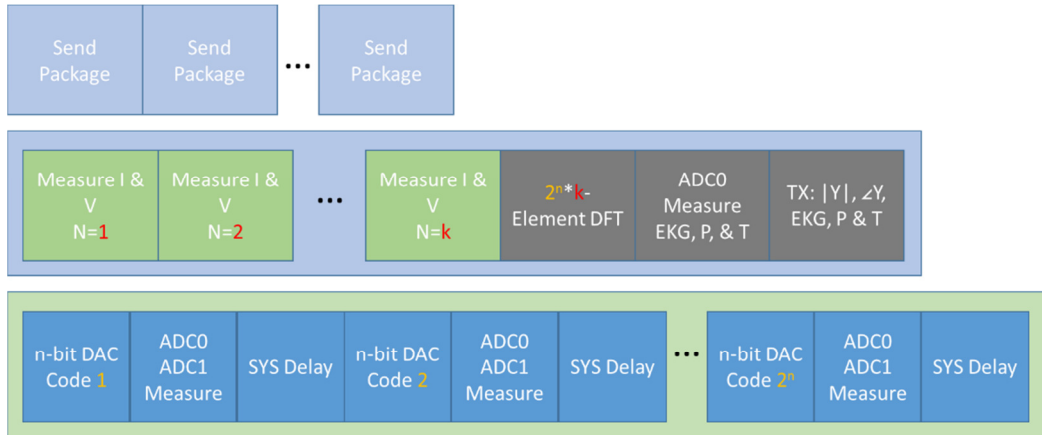


Figure 22: Color-coded Firmware Architecture Depicted in Three Levels.

## 2.7 Wireless Communication



Figure 23: Xbee Wireless Transceiver Modules with Xbee Explorer USB Adapters.

The S1 Xbees operate on the 2.4 GHz 802.15.4 band. Within this band, there are a total of sixteen selectable channels. For each channel, there is a 16-bit personal area network ID (PAN ID) localizing the network. PAN ID may be thought of as a zip code. Lastly, each Xbee

has its own local 16-bit address and a 16-bit destination address for a two-way communication. These local addresses may be thought of as house numbers. The layers hierarchy is generalized in Figure 24. Note, the Xbees can be easily configured with the Digi International XCTU software tool [20].

The way the data transmission works is that the 32-bit and 16-bit integer (int) values are chopped into 8-bit epochs necessary for UART transmission. A line of code is used to check for “0” int values and replace them with “1” int values to avoid confusing the data with a termination code “0”. For example, when a 32-bit value happens to be a “0” value then it would be replaced with a 32-bit “1” value. When a 16-bit value happens to be a “0” then it would be replaced with a 16-bit “1” value. After the check step, the worst-case transmission sequence in terms of bytes is X000 0001 X0 01...X0 01, where “X” is any value from 1 to 255 and “0” is an 8-bit value (if “X” is “0” then the program will catch it since the 32-bit int value would be a “1”). The first eight values are each 8-bit unsigned int values representing the 32-bit admittance phase and magnitude data being transmitted in series. The next series of two-byte packages represent the 16-bit pressure, temperature, and EKG values. Thus  $2N-1$  zeros are needed for a termination package where N represents the number of bytes per integer (four for the admittance data). However, there are corner cases in which the “0” check would fail. For example, a non-zero 16-bit EKG value of 256 would pass the non-zero transmission test. However, because of the way the data is being transmitted (via one byte at a time and in a big endian format) the two EKG bytes being transmitted will have 8-bit unsigned int values of “1” and “0”. Looking at this another way, the value 256 in a 16-bit binary format is 0bx0000 0001 0000 0000. So in terms of two 8-bit int values it is represented as “1” and “0”. This extra “0” will be seen as one of seven termination zeros, and the receiver will misread the frame. Ultimately, the solution for these

corner cases is one termination “1” and seven termination “0”s. The data package composition is shown in Table 1. Given the package update rate of 320 Hz the minimum baud rate required is 61440 bits/s. The baud rate selected for the UART is the maximum setting, 115200 bits/s.

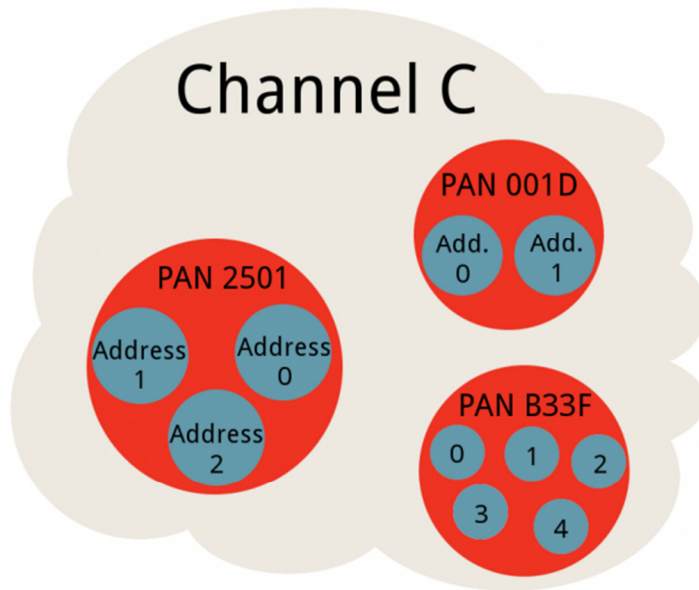


Figure 24 Xbee Network Layers [21].

Table 1: Data Package Composition

Data	Bytes
Admittance Phase	4
Admittance Magnitude	4
Pressure	2
Temperature	2
Temperature	2
EKG	2
Termination One	1
Termination Zeros	7
<b>Total Bytes</b>	<b>24</b>

## 2.8 Admittance Calibration

There are two basic steps for the admittance calibration: 1) apply a phase offset correction and 2) apply gain correction. The phase offset is determined by a resistive sweep. Ideally, the phase offset should be a constant value across the load range i.e. it should be load-independent. However, in practice, there may be small phase fluctuations, sometimes load-dependent, across the entire load range due to system non-linearity and noise. If needed, a lookup table can be used to correct for phase offset [10, 15]. However, since the phase offset variability is small for this instrument, less than  $0.15^\circ$ , a single mean value of  $17^\circ$  is applied for phase correction, Figure 25. Note that the previous generation of instruments required a lookup table since the phase offset varied between 2 and 6 degrees [10, 15]. In this system, the calibration complexity has been reduced by the increased system linearity.

The last step is to perform a first-order linear regression (best-fit line) for the measured resistance vs actual resistance to obtain the gain correction coefficients (slope and offset coefficients). The uncalibrated measurements, calibrated measurements, and post-calibration percent of measurement error for the resistive sweep (from  $300\ \Omega$  to  $1600\ \Omega$ ) are shown in Figure 26. The system is accurate within  $\pm 0.3\%$  for the entire resistive measurement range (a purely resistive measurement).

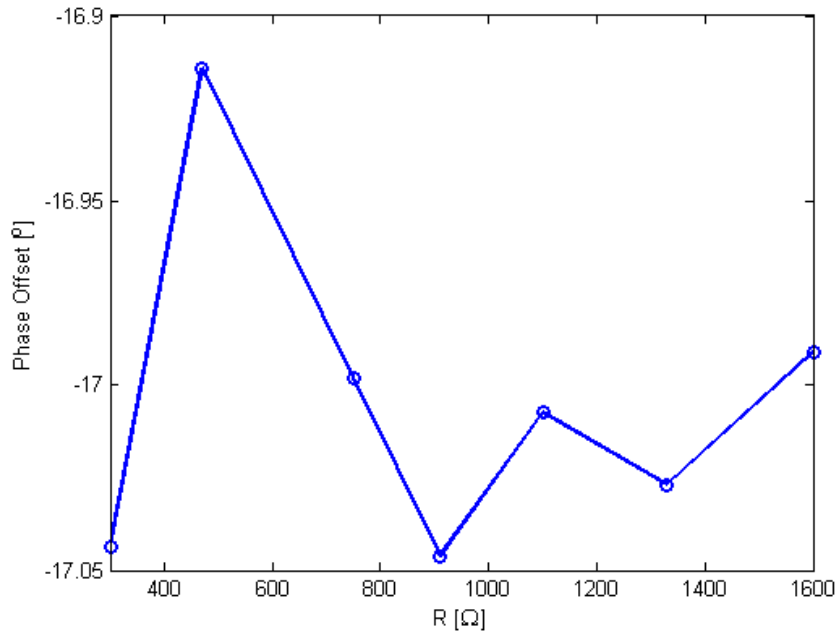


Figure 25: Phase Offset Variability.

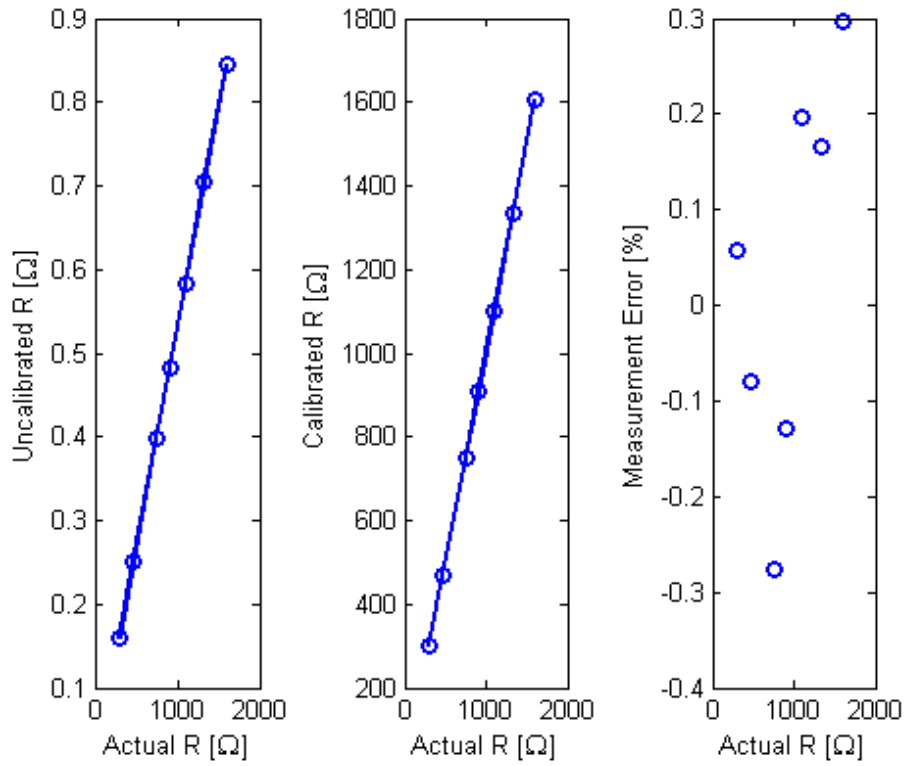


Figure 26: Resistor Sweep Calibration Results.

## 2.9 Thermocouple Calibration

A total of ten different temperature points were used to calibrate the thermocouple sensor (from 22.7 °C to 99.3 °C). The thermocouple was calibrated against the temperature measurements from a Fluke meter. The Fluke meter has measurement accuracy and precision of  $\pm(1\%$  of reading + 1 °C) and 0.1 °C, respectively, Figure 27. Water was heated using a hot plate with a magnetic stirrer to reduce temperature gradients. The average of fifty samples per temperature point was used to determine the calibration curve. To get a linear fit, temperature was plotted against ADC code readout, Figure 28. The linear-fit has an  $R^2$  of 0.99 and the maximum deviation from the linear-fit is 0.65 °C (1.8% of reading). The calibrated temperature channel has a measurement resolution of 0.5 °C.

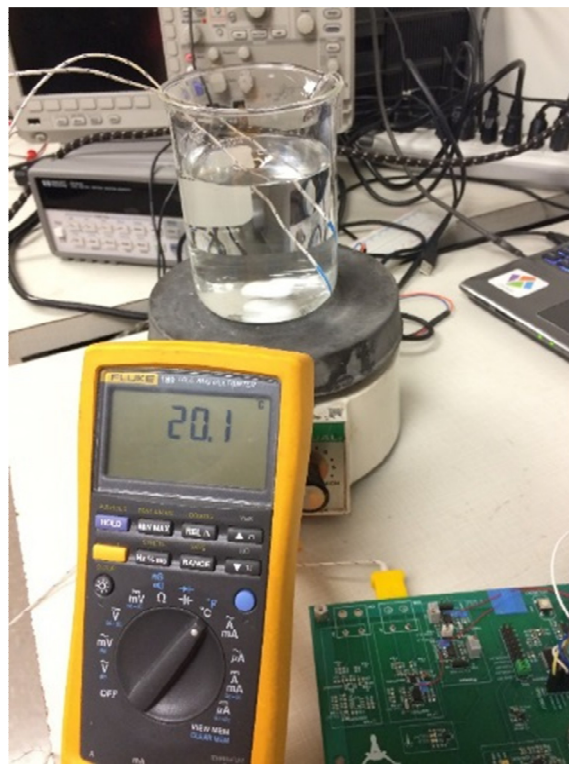


Figure 27: Thermocouple Calibration Experimental Setup.

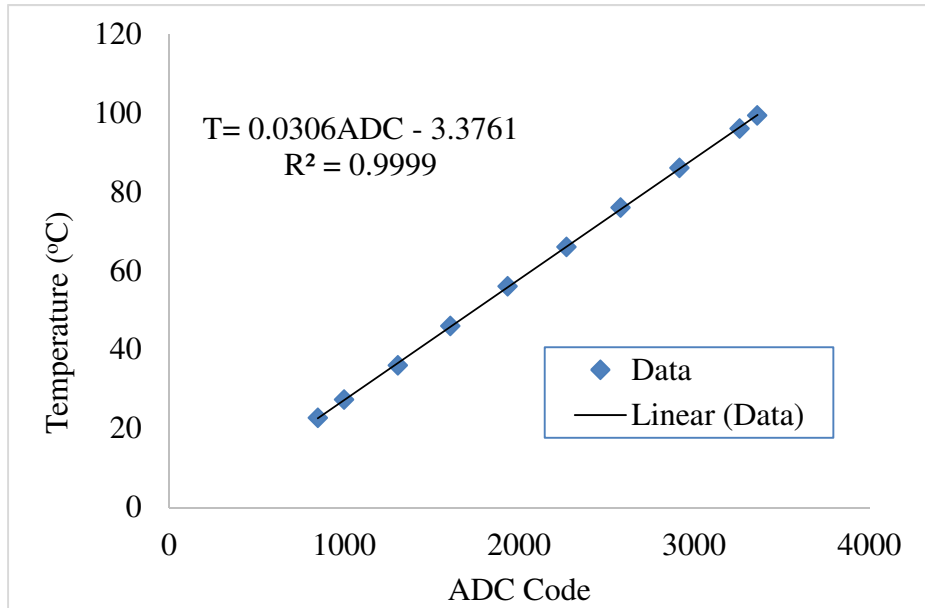


Figure 28: Thermocouple Calibration Curve.

## 2.10 Pressure Calibration

A total of six different forces were used to calibrate the pressure sensor (0 N, 0.049 N, 0.098 N, 0.147 N, 0.196 N, and 0.490 N), Figure 29. The average of 100 samples per force point was used for the calibration curve. To get a linear fit, force was plotted against ADC code readout, Figure 30. The force reading can be readily converted to pressure by using the sensor contact area of 57 mm<sup>2</sup>. The linear-fit has an R<sup>2</sup> of 0.97 and the maximum deviation from the linear-fit is 0.0463 N. Offset and drift were direct results from friction in the mechanical parts. Overall, it is impractical to measure forces less than 0.2 N with this mechanical system.

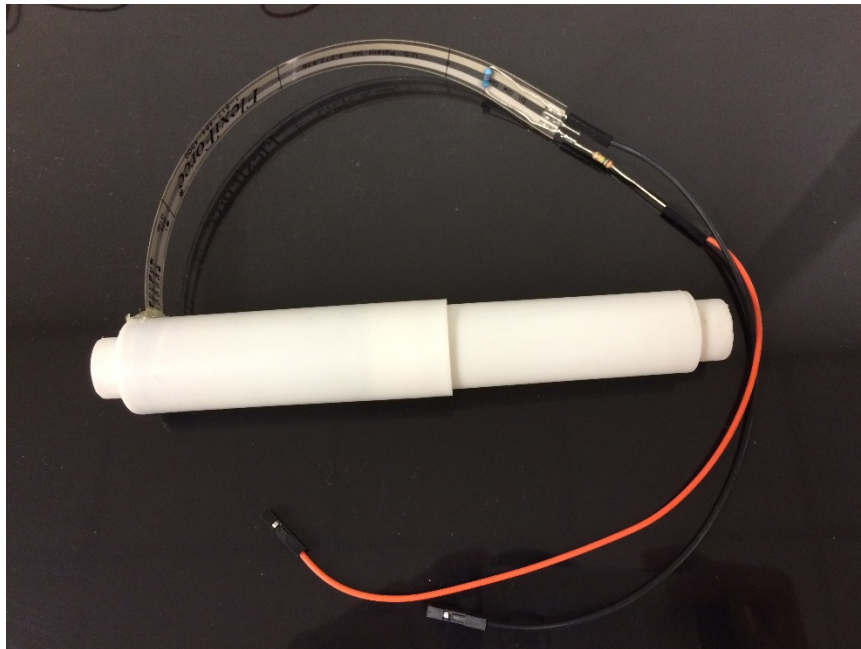


Figure 29: Pressure Sensor System.

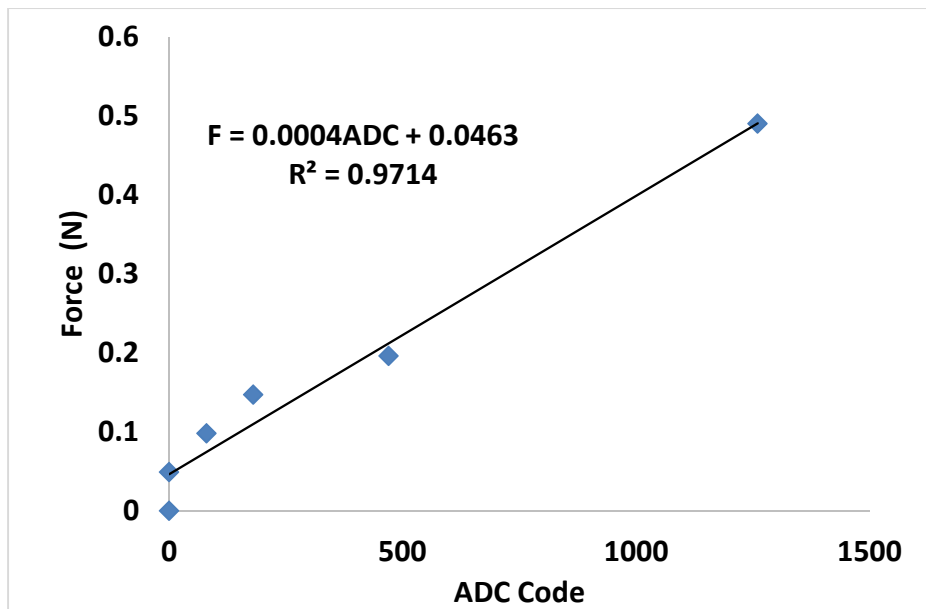


Figure 30: Pressure Calibration Curve.

## 2.11 Breadboard Prototyping

Breadboard prototypes were used to verify the functionality of individual components and system integration prior to printed circuit board (PCB) layout, Figure 31. The breadboard is a great platform to experiment with different novel topologies such as non-inverting versus inverting current sources. With the relative ease of switching components, various op-amps and INAs were tested and compared. However, there are definitely more parasitic elements associated with the breadboard. Typically, there is  $\sim 4\text{pF}$  of stray capacitance between the breadboard nodes.

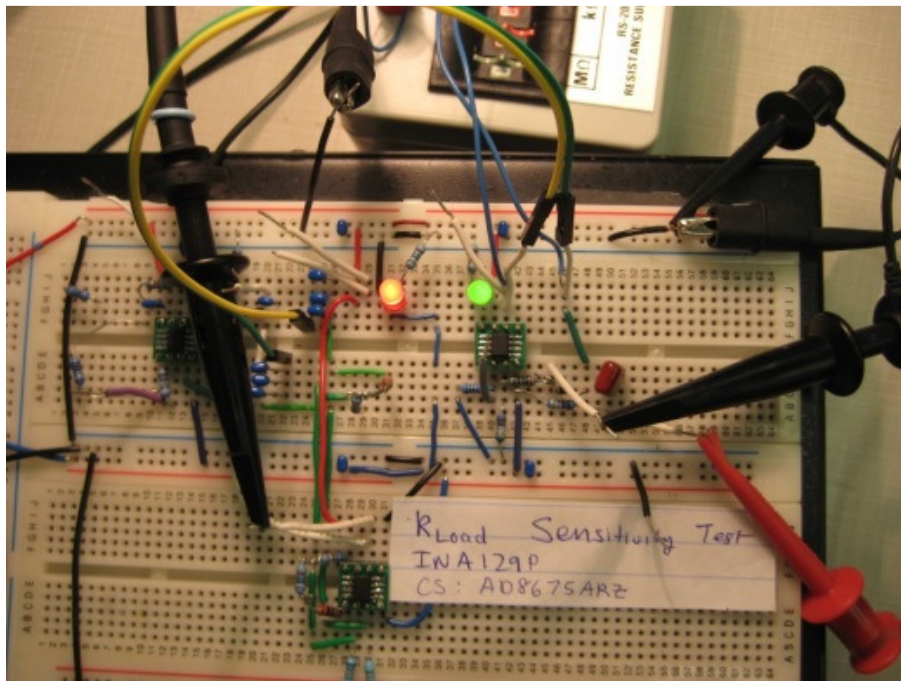


Figure 31: Breadboard Prototype.

## 2.12 PCB Assembly and Electrical Verification

It is important to perform electrical verification in a sequential manner when assembling the PCB. A sequential process allows subsystem isolation making analog debugging more

manageable. Each analog stage was tested and checked against prior calculations to ensure quality, Figure 32.

Managing solder flux is an important aspect of the assembly process. If one is not careful, flux can cause a temperature-dependent drift issue in later tests. A flux pen is preferred for applying flux to reduce excess flux accumulation on the board and alcohol must be used to remove excess flux. The lack of flux is also a potential issue. Exposed pads may get oxidized if left in the open air. The solder flux not only lowers the soldering temperature but also removes the oxidation layer on the pad. Lastly, to avoid “cold solder joints” the pads must be preheated with a soldering iron before applying solder. Proper soldering is necessary to achieve reliability.

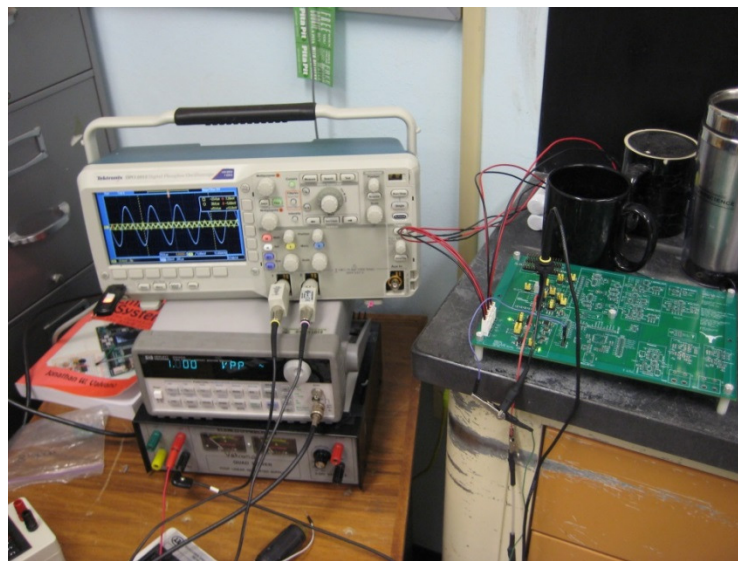


Figure 32: Board Assembly and Electrical Verification

## Chapter 3: System Verification

### 3.1 Admittance RC Load Test

Parallel RC loads were used to test the instrument accuracy and resolution given a complex impedance load. The typical resistive measurement error is less than  $\pm 0.34\%$  and the worst-case error is  $1.7\%$  ( $R=1600\ \Omega$  and  $C=10000\text{pF}$ ), Figure 33. Note “typical” refers to the average of all test points. The worst-case absolute resistive error for the entire range is  $27\ \Omega$  ( $R=1600\ \Omega$  and  $C=10000\text{pF}$ ). On the other hand, the typical capacitive measurement error is  $\pm 1.4\%$  and the worst-case error of  $7\%$  ( $R=1100\ \Omega$  and  $C=100\text{pF}$ ), Figure 34. The worst-case absolute capacitive error for the entire range is  $-140\text{pF}$  ( $R=300\ \Omega$  and  $C=10000\text{pF}$ ). Note that the worst-case absolute error for both the resistive and capacitive measurements occurred when  $C$  was the largest value ( $10000\ \text{pF}$ ). This is perhaps due to a lower SNR for a lower load impedance. A side-by-side study was performed to compare this new design to the previous design of Holt [19]. Data was collected in a similar manner. The Holt system has typical resistive and capacitive measurement errors of  $\pm 0.8\%$  and  $\pm 3\%$  over the same range, respectively. In addition, the worst-case errors of measurements for resistive and capacitive measurements were  $3.9\%$  ( $R=1020\ \Omega$  and  $C=10000\ \text{pF}$ ) and  $26.3\%$  ( $R=300\ \Omega$  and  $C=840\ \text{pF}$ ), respectively, Figures 35 and 36. The worst-case absolute  $R$  and  $C$  measurement error are  $47\ \Omega$  and  $640\ \text{pF}$ , Figures 37 and 38. Clearly, a  $640\ \text{pF}$  of error is unacceptable. The improvement in system linearity has resulted in better accuracy relative to the previous generation, and with the additional benefit of reduced calibration complexity.

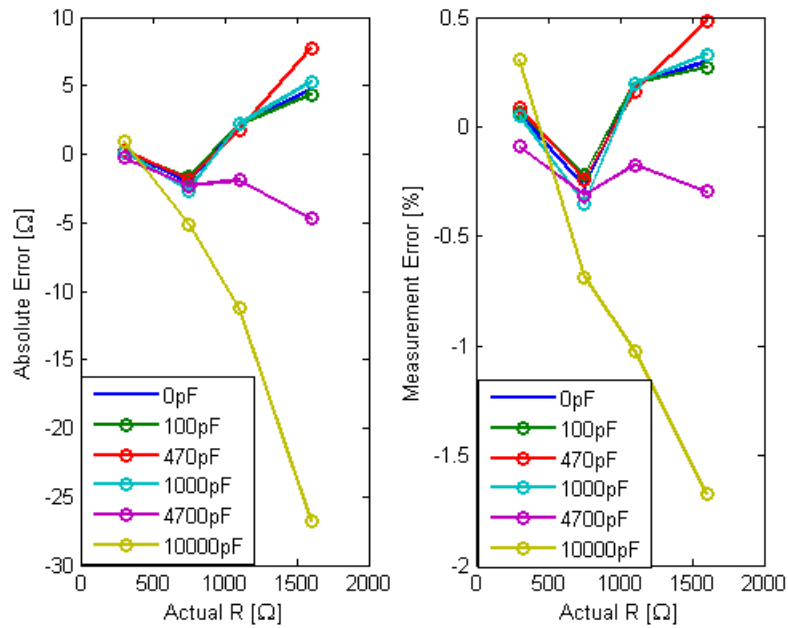


Figure 33: Absolute and Percent of Measurement Errors in Terms of Resistive Error.

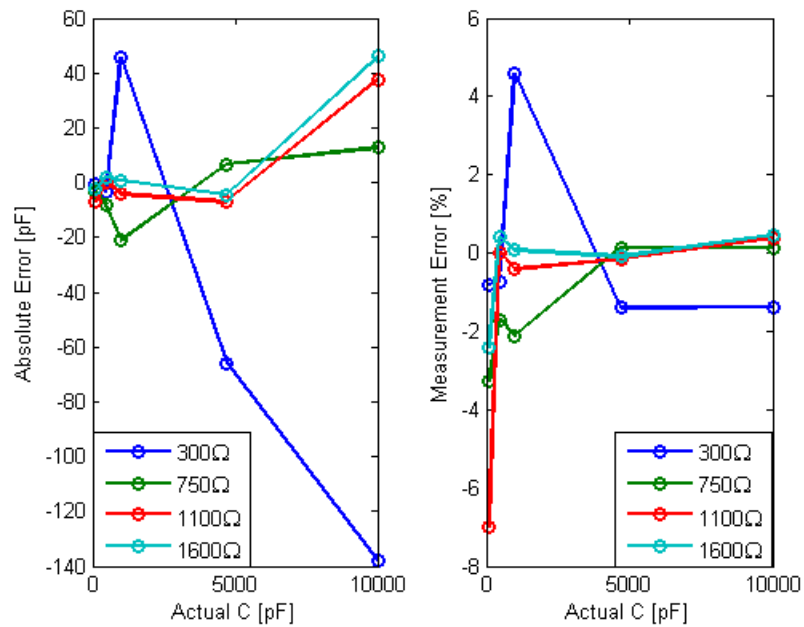


Figure 34: Absolute and Percent Measurement Errors in Terms of Capacitive Error.

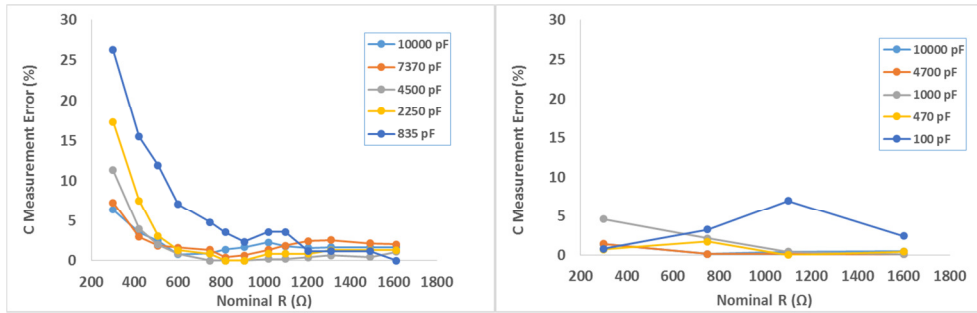


Figure 35: Previous (left) and New (right) Capacitive Percent of Measurement Error.

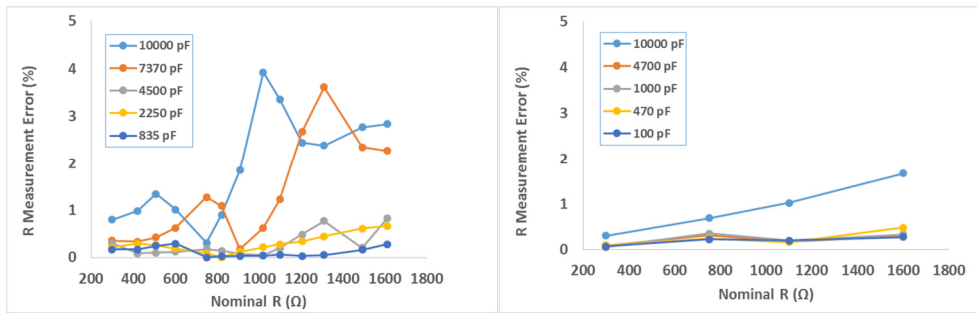


Figure 36: Previous (left) and New (right) Resistive Percent of Measurement Error.

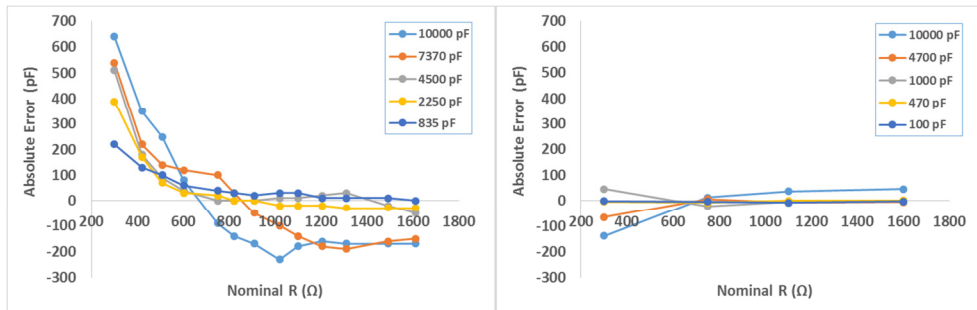


Figure 37: Previous (left) and New (right) Capacitive Measurement Error.

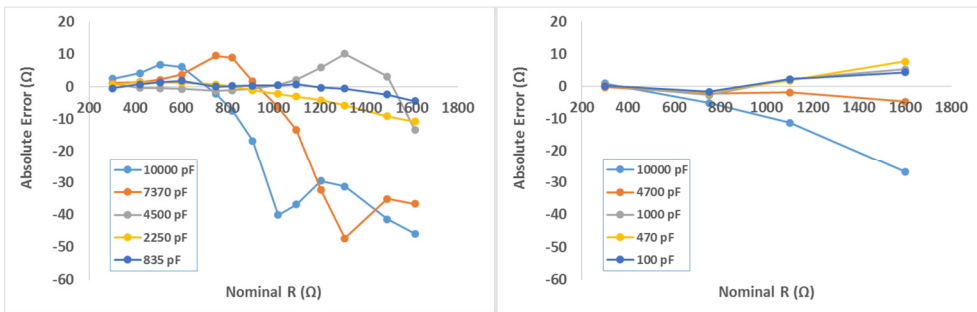


Figure 38: Previous (left) and New (right) Resistive Measurement Error.

### 3.2 EKG Extraction

A function generator was used to generate an artificial EKG test signal. This EKG signal is combined with the 20 kHz DAC output via two resistors (to sum up the signals) in order to test the performance of the analog filtering stages. The aggregate test signal is shown in Figure 39.

The output from the EKG low-pass filter is shown in Figure 40 and the actual recorded waveform using the wireless system is shown in Figure 41. Recall that the overall system sampling rate is 320 Hz.

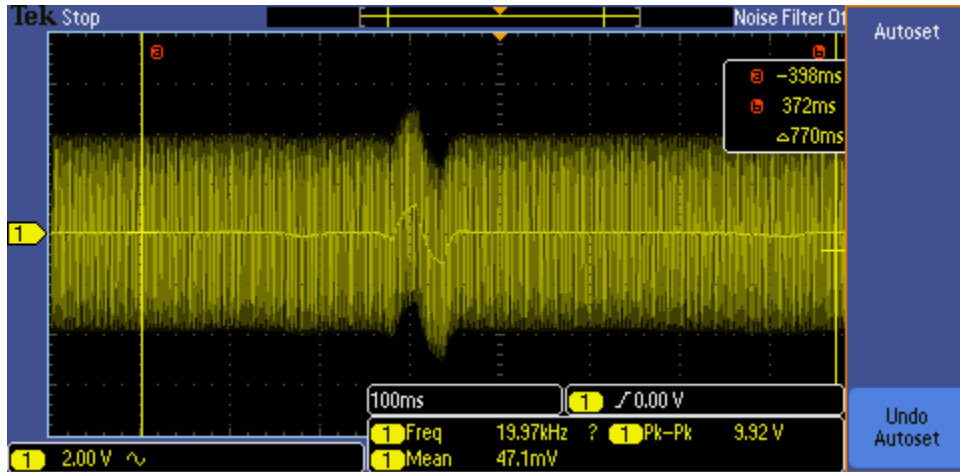


Figure 39: EKG and 20 kHz Admittance Signals.

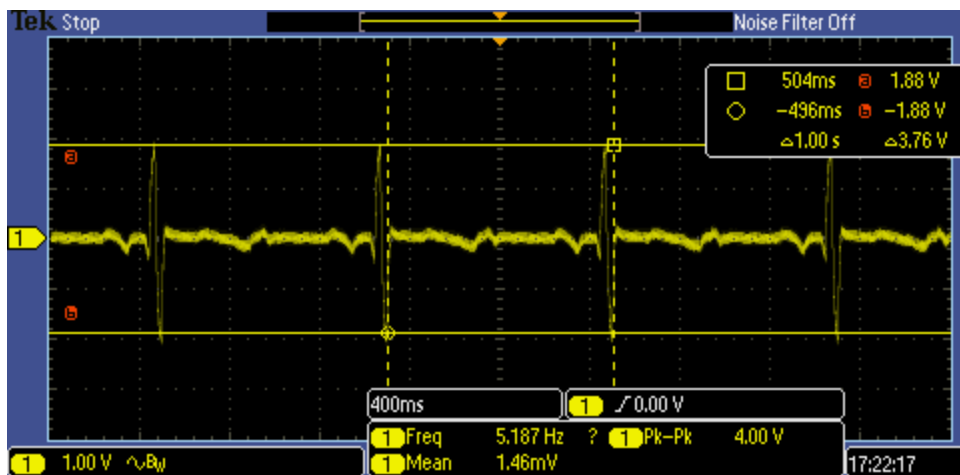


Figure 40: Extracted EKG Signal.

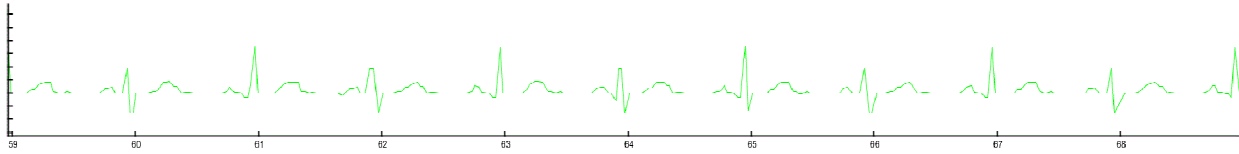


Figure 41: Measured EKG Signal at 320 Hz.

### 3.3 Noise

Using a full scale input corresponding to a 1600  $\Omega$  load, the current and voltage ADC channel noise floors were measured to be approximately -80 dBFS, Figure 42 and 43. Both channels depict an observable 3<sup>rd</sup> harmonic at -60 dBFS. Our measurements indicate that the admittance measurement has a best-case resolution of  $\pm 1 \Omega$  ( $\pm 2\sigma$ ), Figure 44. With a digital filter, this resolution can be improved to  $\pm 0.5 \Omega$  or better.

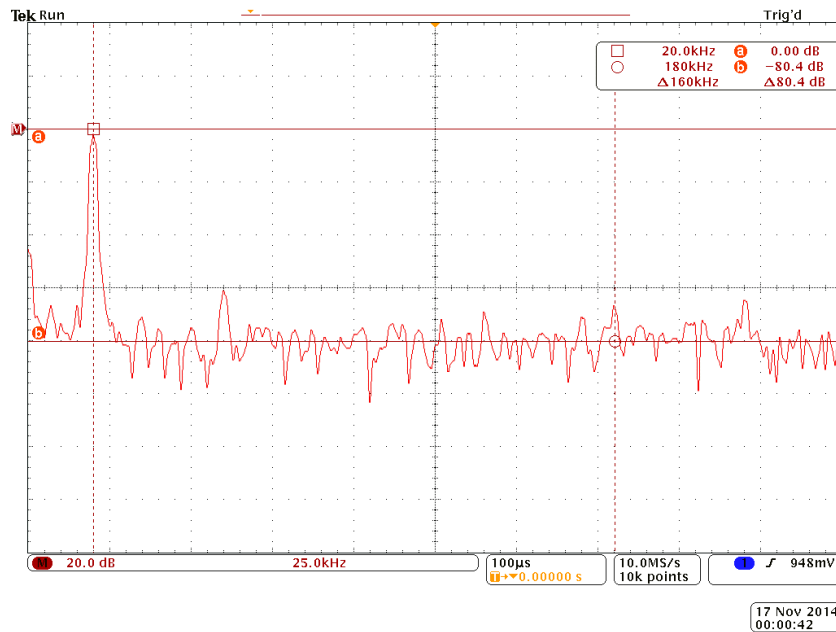


Figure 42: Noise at ADC0 Input.



Figure 43: Noise at ADC1 Input.

A signal-to-noise ratio (SNR) figure of merit for resistive and capacitive measurements are calculated based the following equation:

$$SNR = 20\log_{10} \left( \frac{\text{Mean}}{\text{STD}} \right) \quad (3.1)$$

where the mean is the average and STD is the standard deviation of the measurements. A total of 200 samples were used to determine the SNR for each RC test load. The SNR for the both the resistive and capacitive measurements are depicted in Figure 45 and 46, respectively. The standard deviation is depicted in Figure 44. Note that the worst-case STD for C measurements occurs at the 10000 pF load and the STD increased from 45 pF to 55 pF when the capacitive load increased from 100 pF to 10000 pF, respectively. With the STD staying relatively constant for a 40 dB measurement dynamic range the C SNR will have a 40 dB SNR difference between the lowest and highest capacitive loads. This is confirmed with C SNR plot. The worst-case resistive and capacitive SNR are ~54dB (C=10000 pF) and ~7dB (C=100 pF), respectively. Note that there is a strong correlation between SNR and the equivalent RC impedance for the

resistive measurement. The higher the impedance the higher the resistive SNR. In contrast, the capacitive SNR increases with increasing load capacitance (with R fixed). This makes sense because for the SNR to scale with capacitance the STD has to scale proportionally to the change in capacitance. However, as seen in Figure 44, the STD is relatively constant for the entire capacitive measurement range and thus the C SNR increases with increasing C while R is fixed.

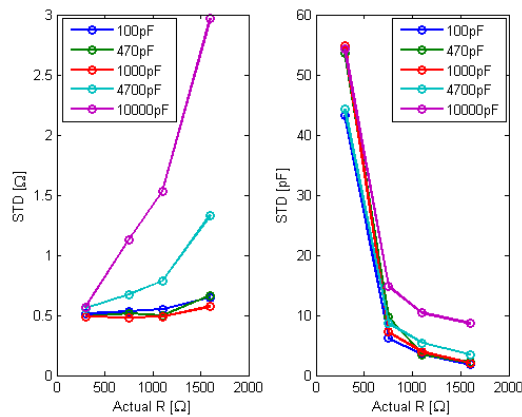


Figure 44: STD for R and C Measurements.

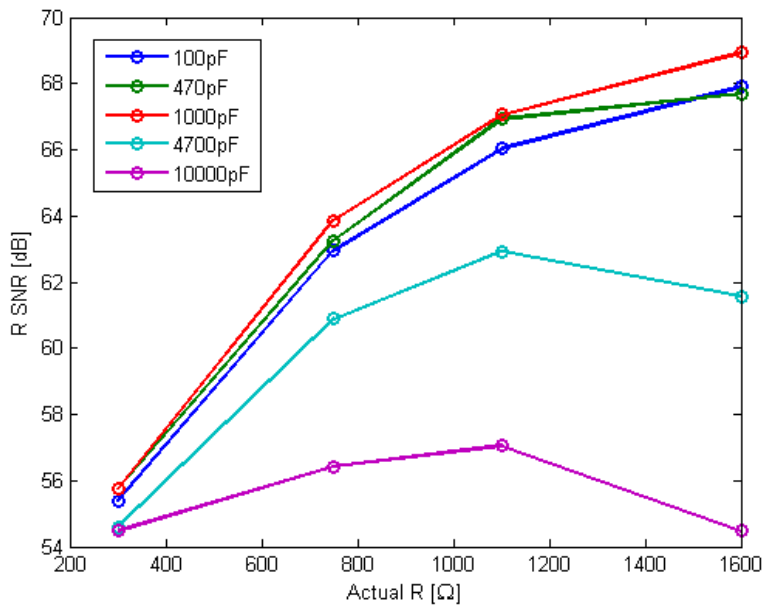


Figure 45: SNR Based on R Measurements.

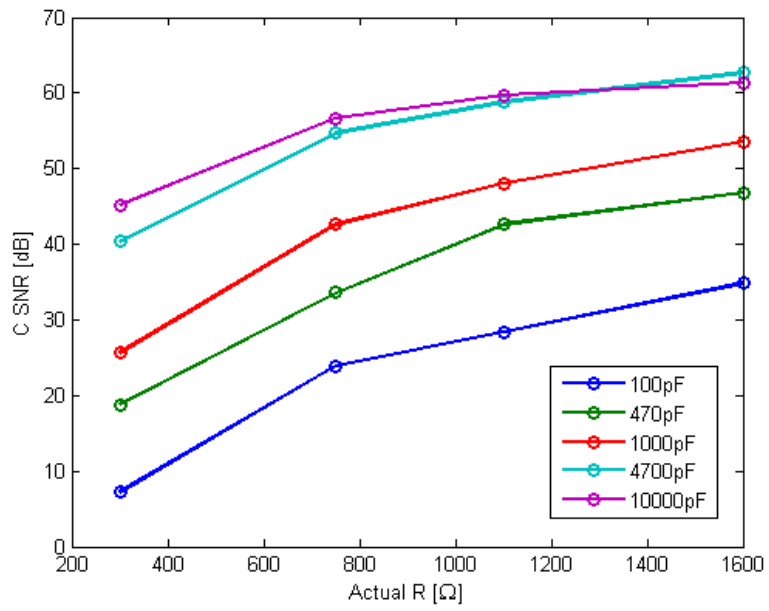


Figure 46: SNR Based on C Measurements.

### 3.4 Wireless Channel Transmission Integrity

The wireless channel was tested for data integrity using a simple ramp function generated via a simple “for loop” on the transmitter side. Values of interest from 0 to 4095 (Note the ADC is 12 bits) were used as test points for this transmission. The way it works is that the receiver reads each new incoming package and compares it to the previously received package and then verifies whether or not the two consecutive data values have a difference of one. Otherwise, it would raise a flag indicating an error. Using this verification step, some transmission corner cases were realized and fixed.

### 3.5 Slew Rate and Headroom

Some of the potential sources for system non-linearity come from the slew rate and headroom requirements. A slow slew rate or inadequate headroom may cause signal distortion, which decreases system linearity. The slew rate (SR) is simply the ratio of change in output voltage  $\Delta V$  to change in time  $\Delta t$ :

$$SR = \frac{\Delta V}{\Delta t} \quad (3.2)$$

For a sinusoidal input the slew rate is:

$$SR = 2\pi * f * V_p \quad (3.3)$$

where  $f$  is the frequency and  $V_p$  the peak voltage. In general, the previous equation can be used to calculate the SR required for the current source and INA stages. For the current source stage, a more detailed equation for the SR is:

$$SR = 2\pi * f * R_{tol} * I_p \quad (3.4)$$

where  $I_p$  is the peak current (140  $\mu\text{A}$ ) and  $R_{\text{tol}}$  is the total load resistance including the current sense (200  $\Omega$ ) and set (1 k $\Omega$ ) resistors. Since the maximum input load is 1.6 k $\Omega$   $R_{\text{tol}}$  is 2.8 k $\Omega$ . This means that the minimum SR required for the current source op-amp is 49 mV/ $\mu\text{s}$ . Typically, a SR of at least five times the minimum requirement is required to minimize high-order non-linearity effects. The op-amp used has a SR of 2.5 V/ $\mu\text{s}$  or 51 times the requirement. Thus SR verification is not crucial for the current source stage.

For the INA stage, the SR is:

$$\text{SR} = 2\pi * f * R_L * I_p * G_{\text{INA}} \quad (3.5)$$

where  $G_{\text{INA}}$  is the gain of the INA and  $R_L$  is the input load resistance. The worst-case minimum slew rates required for the current and voltage channels are 1.4 V/ $\mu\text{s}$  (200 $\Omega$ \*140 $\mu\text{A}$ \*400\*2 $\pi$ \*20kHz) and 1.1 V/ $\mu\text{s}$  (1600 $\Omega$ \*140 $\mu\text{A}$ \*40\*2 $\pi$ \*20kHz), respectively. Since only the typical SR is listed in the INA datasheet (4V/ $\mu\text{S}$ ) tests were performed to verify the actual SR. Using a 20 kHz, 500mVpp square wave the INA slew rates were verified for both the current and voltage channels.

The measured INA slew rates are 4.86 V/ $\mu\text{s}$  (20.6V/4.24 $\mu\text{s}$ ) and 5.18 V/ $\mu\text{S}$  (23.2V/4.48 $\mu\text{s}$ ). Note that since the INA for the current channel has a higher gain of 400 V/V compared to the voltage channel INA gain of 40 V/V, the output voltage is saturated at 23.2Vpp, Figure 47. This implies 800 mVpp of headroom given the  $\pm 12\text{V}$  rails. Nevertheless, this does not affect the SR measurements. Note that the SR usually increases proportionally with the INA gain. So the higher SR measured for the current channel is not surprising.

The worst case headroom requirement for the INA is 1.4 V (from the datasheet) thus the maximum input load before clipping is  $(12V-1.4V)/40/140\mu A=1893\Omega$ . That is the theoretical limit of input load. However, in practice, as the input load approaches this limit, high-order effects may have some significant effects on the output waveform. For the voltage channel, with an input load range from  $300\ \Omega$  to  $1600\ \Omega$ , the headroom is not an issue given  $\pm 12\ V$  rails,  $140\ \mu A_{peak}$  stimulation current, and INA gain of  $40\ V/V$ . The current channel has a fixed load of  $200\ \Omega$  and a nominal INA gain of  $400\ V/V$ . The estimated maximum peak output voltage for the voltage and current channels are  $1600\Omega*140\mu A*40 = 9\ V$  and  $200\Omega*140\mu A*400 = 11.2\ V$ , respectively. Note that the current channel gain of  $400\ V/V$  is a nominal gain setting. The effective gain will be determined by the GBWP also. In practice, the actual gain is around  $370\ V/V$  at  $20\ kHz$  due to some attenuation from the INA  $f_{3db}$  pole located at  $50\ kHz$ . Thus the maximum peak voltage for the current channel is  $200\Omega * 140\mu A * 370 = 10.36\ V$ . The worst-case headroom requirement for the INA is  $1.4\ V$ , so the headroom is not an issue given  $\pm 12\ V$  supply rails.

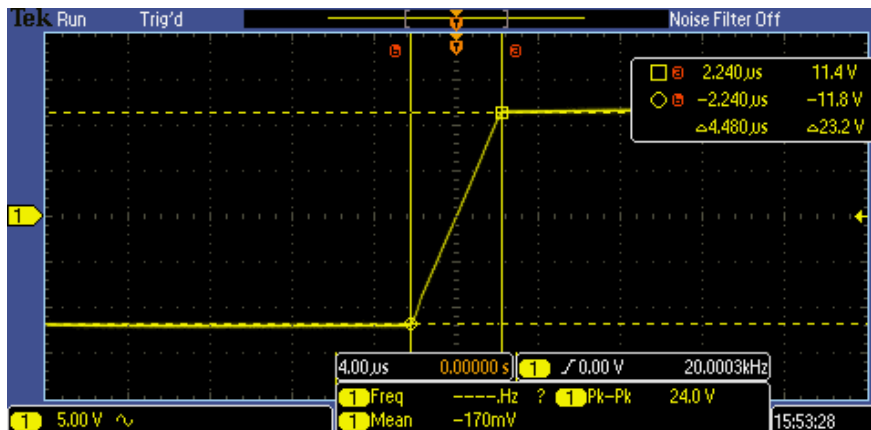


Figure 47: Measuring INA SR Using the Rising Edge of a 20 kHz Square Wave.

### 3.6 CMRR

Measured in decibels (dB), the common mode rejection ratio (CMRR) is an integral specification of any bio-impedance system. In a sense, it is the first line of defense against common mode noise that is ubiquitous in biological systems. An experiment was conducted to study the effect of component mismatch on the instrumentation amplifier (INA) CMRR as function of frequency for different INA gain configurations. The basic experimental setup is shown in Figure 48. Note that the test signal is a 100 mVpp sinusoid provided by a function generator. For each gain setting, both the common mode and differential mode gains were measured as a function of input frequency (60 Hz, 1 kHz, 10 kHz, 20 kHz, and 50 kHz). The CMRR is defined as follows:

$$\text{CMRR}=20\log\left(\frac{A_d}{A_{cm}}\right) \quad (3.6)$$

where  $A_d$  and  $A_{cm}$  are the differential and common mode gains, respectively. Typically, monolithic INAs have very good CMRR at low frequencies. However, a major source of CMRR degradation arises from component mismatch. The RC high-pass filter stage immediately before the INA stage, for DC blocking, presents a major source of component mismatch, degrading the INA CMRR. The high-pass filter under test was an RC filter with  $C=300$  nF (1% tolerance) and  $R=1$  M $\Omega$  (0.1% tolerance). At 20 kHz, the difference between gains of 40V/V and 200V/V is ~10 dB of CMRR, Figure 49. The results reinforce the need for a moderate INA gain setting and good component matching.

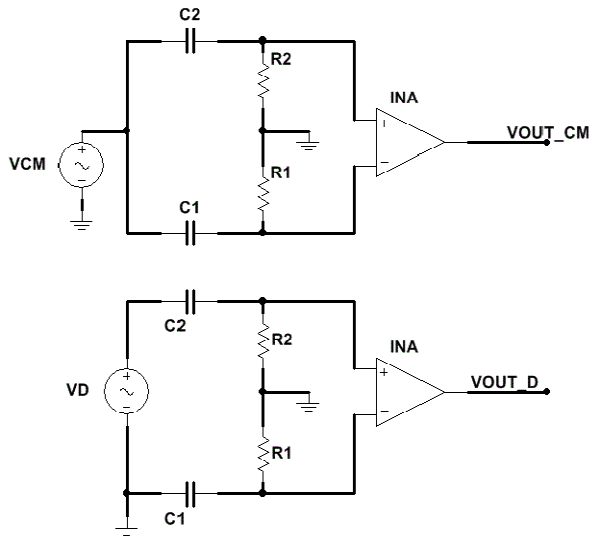


Figure 48: CMRR Measurement Setup for Common (top) and Differential (bottom) Modes.

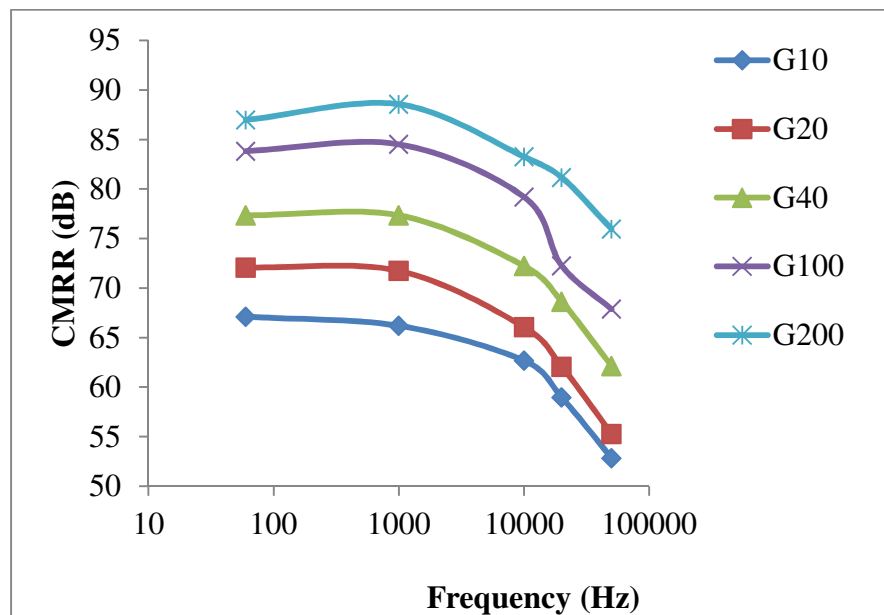


Figure 49: CMRR Frequency Sweep.

### 3.7 Frequency Jitter

The current source frequency stability is of great significance. An experiment was performed to measure the frequency jitter of the current source. The frequency jitter was determined by measuring the control voltage at the negative terminal of the voltage-controlled current source. The inverting terminal of the non-inverting op-amp is the node that ultimately sets the current into the load. A total of six sinusoidal periods were averaged for each frequency measurement. The measurements showed that the current source frequency has a jitter of  $\pm 157$  Hz, Table 2. Note: 280 mVpp corresponds to approximately 100  $\mu$ Arms. Using the frequency jitter data, worst-case measurement error due to clock jitter can be estimated using these equations:

$$Y_{\text{mea}} = \frac{I_{\text{mea}}}{V_{\text{mea}}} \quad (3.7)$$

$$\phi_{\text{mea}} = \text{atan} \left( \frac{\text{Im}(Y_{\text{mea}})}{\text{Re}(Y_{\text{mea}})} \right) \quad (3.8)$$

$$C_{\text{mea}} = \frac{|Y|_{\text{mea}} \text{Sin}(\phi_{\text{mea}})}{2\pi * 20\text{kHz}} \quad (3.9)$$

$$R_{\text{mea}} = \frac{1}{|Y|_{\text{mea}} \text{Cos}(\phi_{\text{mea}})} \quad (3.10)$$

where the subscript “mea” represents the actual measured values based on the actual frequency. For the capacitive measurement the error arises from the assumption of a constant 20 kHz frequency reference. Knowing that the worst-case frequency jitter is roughly  $\pm 150$  Hz ( $\pm 2\sigma$ ), the worst-case measurement error can be modeled. Based on the frequency jitter model, the predicted worst-case capacitive measurement error is  $\pm 75$  pF for a 10000 pF load independent of

the parallel resistive load. Interestingly, the resistive measurement error from the model is not sensitive to frequency jitter. This is because the resistance calculation does not require a frequency reference. Overall, the modeling results provided some explanations to the potential capacitive load dependent measurement errors.

Table 2: Current Source Frequency Jitter Measurements.

Test Number	Frequency (kHz)	Pk-Pk (mV)
1	20.03	280
2	19.98	280
3	19.99	280
4	19.94	280
5	19.88	280
6	20.00	280
7	20.09	280
8	20.09	280
9	20.09	280
10	20.13	280
<b>Average</b>	20.022	280
<b>2σ</b>	0.157423703	0

### 3.8 Power Consumption

The power consumption was verified as a sanity check. Current was measured at the battery input stage. The analog stage alone consumes roughly 70 mA off the  $\pm 14.8$  V rails. The wireless module and MCU combined consume roughly 100 mA off the +7.4 V rail. The Xbee module alone consumes 60 mA of that 100 mA. Therefore, the total power consumed is  $7.4V \cdot 4 \cdot 70mA + 7.4V \cdot 100mA = 2.81$  W. Ultimately, one of the four batteries has to supply a total of 170 mA and this means that the overall system has an operating range of thirteen hours (2200mAh/170mA).

## Chapter 4: Conclusion

### 4.1 New Measurement System

The new bio-impedance measurement system design was motivated by the limited performance of the previous bio-impedance measurement systems. The immediate consequence of these limitations was made obvious from the preliminary rat ablation studies, which yielded inconclusive results. Given the much wider input range requirement, a new system with improved linearity was required. With virtually no size or power constraints the new system was designed to be high-performance. Key performance metrics comparing the new and previous systems are summarized in Table 3. Some of the most noticeable improvement is in the capacitive measurement errors, where the worst-case absolute and percent of measurement errors were improved by roughly four-fold. The system linearity was much better than the target with less than  $0.15^\circ$  phase variation for the entire input load range. Compared to the maximum phase variation of  $7^\circ$  in previous systems [10, 15] this is a significant linearity improvement. The improved linearity is partly due to real-time current measurement. The improved system linearity makes the calibration step much easier requiring only a constant phase offset correction compared to the table lookup calibration step required for previous systems.

Table 3: System Performance Summary.

	<b>Target</b>	<b>Achieved</b>	<b>Previous</b>
R Measurement Error (%)	<2	<2	<4
C Measurement Error (%)	<5	<7	<27
Absolute C Error (pF)	<100	<140	<640
Phase Variation ( $^\circ$ )	<1	<0.15	<7

## 4.2 Unresolved Issues

There are a number of unresolved issues on the first revision. The most critical issue is the low resolution of the pressure sensor. This problem is partly due to mechanical friction originating from the spring-loaded device moving parts. This problem amounts to significant measurement drift that makes measuring forces of less than 0.2 N impractical. This problem will need to be addressed with better alternative mechanical designs and more sensitive pressure transducers. An optical pressure sensor may prove to be a better alternative.

At present, the system takes a significant portion of CPU cycles for the admittance measurements and data processing. The consequence is that the EKG is being sampled at 320 Hz. To avoid aliasing, the EKG filter corner frequency will need to be lowered to at least 160 Hz or less.

## 4.3 Future Direction

Even though the new measurement system has made significant performance improvements there is still some room for optimization. Frequency jitter due to noise coupling can be reduced with a more careful design layout. Currently, the first board revision has only two layers. With four layers, the board can have more layers for electromagnetic shielding and optimal trace routing. Also, the more components the board has the more ground noise there will be. At the present 2.8 W power consumption, there is a significant ground current. In addition, the first board revision has many jumpers giving the designer more flexibility but they may have also increased the noise coupling. Lastly, the PCB area is also an important factor since it acts like an antenna. A smaller revised PCB could further improve noise performance. With these fixes implemented in the second revision, perhaps all of the target specifications will be met and

*in vivo* experiments can be performed to verify the measurement system under real-life test conditions.

## References

- [1] *Heart Arrhythmia*. (n.d.). Retrieved November 10, 2014, from <http://health.usnews.com/health-conditions/heart-health/heart-arrhythmia/overview>
- [2] *When Your Heart Rhythm Isn't Normal*. (n.d.). Retrieved November 10, 2014, from <http://www.webmd.com/heart-disease/guide/heart-disease-abnormal-heart-rhythm#1>
- [3] *What Is Arrhythmia?* (n.d.). Retrieved November 10, 2014, from <http://www.healthline.com/health/arrhythmia#Overview1>
- [4] S. I. Fox, *Human Physiology*, 9<sup>th</sup> ed., New York, NY: McGraw-Hill, 2006.
- [5] D. Haemmerich, "Biophysics of radiofrequency ablation," *Crit. Rev. Biomed. Eng.* **38**,53–63, 2010.
- [6] J. Cinca, M. Warren, A. Rodriguez-Sinovas, M. Tresanchez, A. Carreno, R. Bragos, O. Casas, A. Domingo, and J. Solernoloer, "Passive transmission of ischaemic ST segment changes in low electrical resistance myocardial infarct scar in the pig," *Cardiovasc. Res.* **40**, 103-112, 1998.
- [7] O. Casas, R. Bragos, P.J. Riu, et al., "In vivo and in situ ischemic tissue characterization using electrical impedance spectroscopy," *Ann. NY Acad. Sci.* **873**, 51–58, 1999.
- [8] E. Larson, "Admittance measurement for assessment of cardiac hemodynamics in clinical and research applications," University of Texas, Austin, 2012.
- [9] E. Larson, J.A. Pearce, M.D. Feldman, "Analysis of the Spatial Sensitivity of Conductance / Admittance Catheter Ventricular Volume Estimation," *IEEE Transactions on Biomedical Engineering*, **60**, 1-9, 2013.
- [10] L. Holt, "Implantable Intracardiac Bioimpedance System," University of Texas, Austin, 2014.
- [11] J. Porterfield, "Admittance measurement for early detection of congestive heart failure," University of Texas, Austin, 2010.
- [12] J. Porterfield, A. Kottam, K. Raghavan, et al., "Dynamic Correction for Parallel Conductance, GP, and Gain Factor,  $\alpha$ , in Invasive Murine Left Ventricular Volume Measurements. Journal of Applied Physiology," *J. Appl. Physiol.* **107**, 1693-1703, 2009.

- [13] J. Porterfield, E. Larson, J. Jenkins, et al., "Left Ventricular Epicardial Admittance Measurement for Detection of Acute LV Dilation," *J. Appl. Physiol.* **110**, 799-806, 2010
- [14] S. Grimnes and Ø. G. Martinsen, *Bioimpedance and Bioelectricity Basics*, 2<sup>nd</sup> ed., Waltham, MA: Academic Press, 2008.
- [15] K. Loeffler, "Development of an implantable system to measure the pressure-volume relationship in ambulatory rodent hearts," University of Texas, Austin, 2012.
- [16] *Sallen-Key filters*. (n.d.). Retrieved November 10, 2014, from <http://www.analog.com/static/imported-files/tutorials/MT-222.pdf>
- [17] *Manual on the Use of Thermocouples in Temperature Measurement*, 4th ed., ASTM., 48–51, 1993.
- [18] *Getting Started with the Tiva™ TM4C123G LaunchPad Workshop*. (n.d.). Retrieved November 10, 2014, from [http://software-dl.ti.com/trainingTTO/trainingTTO\\_public\\_sw/GSW-TM4C123G-LaunchPad/TM4C123G\\_LaunchPad\\_Workshop\\_Workbook.pdf](http://software-dl.ti.com/trainingTTO/trainingTTO_public_sw/GSW-TM4C123G-LaunchPad/TM4C123G_LaunchPad_Workshop_Workbook.pdf)
- [19] *Stellaris LM4F120 LaunchPad Debug How To*. (n.d.). Retrieved November 10, 2014, from [http://processors.wiki.ti.com/index.php/Stellaris\\_LM4F120\\_LaunchPad\\_Debug\\_How\\_To](http://processors.wiki.ti.com/index.php/Stellaris_LM4F120_LaunchPad_Debug_How_To)
- [20] *XCTU*. (n.d.). Retrieved November 10, 2014, from <http://www.digi.com/products/wireless-wired-embedded-solutions/zigbee-rf-modules/xctu>
- [21] *Exploring XBees and XCTU*. (n.d.). Retrieved November 10, 2014, from <https://learn.sparkfun.com/tutorials/exploring-xbees-and-xctu>